Journal of the Meteorological Society of Japan

EARLY ONLINE RELEASE

The DOI for this manuscript is
DOI:10.2151/jmsj.2025-012
J-STAGE Advance published date: January 15, 2025
The final manuscript after publication will replace the preliminary version at the above DOI once it is available.

Representation of Quasi-Biennial Oscillation in JRA-3Q

Hiroaki NAOE[1]**, Chiaki KOBAYASHI,**

Meteorological Research Institute, Japan Meteorological Agency, Tsukuba, Japan

Shinya KOBAYASHI, Yuki KOSAKA,

Numerical Prediction Development Center, Japan Meteorological Agency, Tsukuba, Japan

and

Kiyotaka SHIBATA,

Kochi University of Technology, Kami, Japan

December 26, 2024

Revised, to be submitted to JMSJ

----

1) Corresponding author: NAOE Hiroaki, Meteorological Research Institute, 1-1, Nagamine, Tsukuba 305-0052 JAPAN

Email: hnaoe@mri-jma.go.jp

Tel: +81-29-853-8595

Abstract

This study evaluates the representation of the quasi-biennial oscillation (QBO) in zonal wind and temperature in Japanese Reanalysis of Three Quarters of a Century (JRA-3Q). We examine the temporal consistency of the QBO between the post- and pre-satellite eras, by comparing it with other reanalyses and observations of radiosonde and satellite data. Here, we quantify the disagreement between the post- and pre-satellite eras using the background spectrum based on the post-satellite era. In the satellite era, the QBO amplitudes of the zonal wind and temperature at 20–30 hPa are somewhat reduced in JRA-3Q by approximately 8% and 4%, respectively, compared with other reanalyses. However, the JRA-3Q QBO from the early 1960s and before is substantially degraded, falling below the 95% confidence level. The representation of the JRA-3Q annual oscillation in the equatorial stratosphere is improved, whereas that in the pre-satellite era in the Japanese 55-year Reanalysis completely disappears due to unrealistically strong damping. The zonal asymmetry of the zonal wind QBO amplitude is characterized by a wave-1 structure with a magnitude of approximately 1 m s^{-1} in the middle-to-upper stratosphere and a larger amplitude in the central Pacific in the lower stratosphere, consistent with previous studies. The disconnection of temperature QBO-amplitude anomalies between the lower and middle stratosphere is observed in some reanalyses, whereas those in JRA-3Q exhibit an eastward tilt with height, although underlying cause of these anomalies remains unclear.

In short, QBOs remain a challenge especially with high-resolution models. 1) How to tune the high-resolution-version QBOs to match lower-resolution versions set up for climate when restricted to outputs over the short numerical weather prediction timescales. 2) How to sustain QBO amplitudes further into the past with limited data availability. This study has a broader applicability than simply development of reanalysis systems, and understanding and implications of their limitations.

Keywords reanalysis; quasi-biennial oscillation; wavelet analysis; JRA-3Q;

1. Introduction

The dominant mode of variability in the tropical lower-to-mid stratosphere is the quasi-biennial oscillation (QBO), which is approximately zonally symmetric and is characterized by alternating westerly and easterly phases propagating downward in the equatorial stratosphere with a frequency of 2–3 years (Baldwin et al. 2001; Anstey et al. 2022b). The QBO significantly influences the entire stratosphere and even the troposphere through the troposphere-stratosphere coupling. In the tropical upper stratosphere, the semi-annual-oscillation (SAO) (e.g., Ern et al. 2021) and annual oscillation (ANN) are dominant, although a small component of QBO variability extends into the upper stratosphere and mesosphere.

The reanalysis integrates model data with observations worldwide to produce a high-quality climate dataset using a consistent, state-of-the-art data assimilation system. Modern reanalyses significantly contribute to the verification of phenomena such as the QBO. According to a comparison of reanalyses by Randel et al. (2004), significant differences were documented in the representation of the stratosphere among different analyses. Subsequent, continuous improvements in reanalyses led to considerably smaller differences in QBO representation among modern reanalyses (Kawatani et al. 2016). Recently, the Stratosphere–troposphere Processes And their Role in Climate (SPARC) (2022) conducted a coordinated intercomparison of reanalysis data sets, focusing on key diagnostics including the QBO, and it aimed at elucidating the underlying cause of these discrepancies. Wind profiles from tropical radiosonde stations constitutes the primary observational constraint for the QBO in the reanalysis, whereas the global coverage provided by satellite observations since the late 1970s has some impacts on the tropical stratosphere (Anstey et al. 2022a). Thus, it is interesting to assess the reliability of QBO representation in the state-of-the-art reanalysis for the pre-satellite era and to evaluate the extent to which the modern reanalysis realistically captures QBO by comparing it with independent observations. This evaluation is crucial for remaining issues among reanalyses.

Modeling studies employing general circulation models (GCMs), have attempted to realistically simulate the QBO. Takahashi (1996) first simulated QBO-like oscillations with a 1.5-year period using a GCM with a spectral truncation of T21 and 60 vertical layers. This model utilized a vertical resolution of 500 m in the upper troposphere and lower stratosphere, along with reduced horizontal diffusion in those regions. Subsequently, QBO-like oscillations have been produced in many models (e.g., Hamilton et al. 1999; Scaife et al. 2000; Giorgetta et al. 2002; Shibata and Deushi 2005). Watanabe et al. (2008) demonstrated a spontaneous QBO-like oscillation in their simulations without employing parameterizations for gravity wave drag (GWD). Instead, they incorporated convection, topography, instability, and adjustment processes. There were three modifications to facilitate the development of QBO-like oscillations in general circulation and chemistry-climate models (e.g., Shibata and Deushi 2005; Takahashi 1996): 1) employing fine vertical layers in the upper troposphere and stratosphere, 2) reducing horizontal diffusion further below standard values in the stratosphere and above, and 3) replacing the Rayleigh friction used in earlier versions by introducing the nonorographic GWD scheme proposed by Hines (1997).

Over two decades after the first simulated QBO-like oscillation, significant uncertainty remains regarding the requirements for achieving a QBO in free-running atmospheric GCMs and Earth system models (ESMs) without data assimilation. These models depend on parameterized nonorographic GWD, often tuned to improve model performance in the stratosphere and mesosphere, including the QBO, and to provide much of the QBO wave forcing. To improve the simulation of tropical stratospheric variability in GCMs/ESMs, the SPARC/QBO initiative (QBOi) conducted a series of coordinated experiments (Butchart et al. 2018). They found that free-running models may either underestimate or overestimate the QBO amplitude and exhibit significantly larger quantitative and qualitative discrepancies in their representation of the QBO compared to various reanalyses (Bushell et al. 2022; Schenzinger et al. 2017). This implies that even with high-resolution models accurately simulating a realistic QBO is still challenging.

Until recently, specifically before the 2010s, a nonorographic GWD parametrization was incorporated into several reanalysis models including the Climate Forecast System version 2 (CFSv2; Saha et al. 2014), European Centre for Medium-Range Weather Forecasts (ECMWF) 20th century reanalysis (ERA-20C; Poli. 2016), and the Modern-Era Retrospective Analysis for Research and Applications (MERRA; Rienecker et al. 2011). These reanalyses managed to resolve the impacts of small-scale contribution from gravity waves (Table 2.7 of SPARC 2022, which summarized GWD parameterizations used in the forecast models of the reanalysis). However, introducing a nonorographic GWD parametrization did not guarantee the generation of a realistic QBO (Anstey et al. 2022a). This means that especially with high-resolution models, reanalysis QBOs remain a challenge as we have yet to solve the problem of tuning over the short numerical weather prediction (NWP) timescales that we can afford to run, but the goal is accurate prediction of oscillation characteristics that can only be evaluated after many years of simulation (or analysis).

The first reanalysis QBO represented realistically using a self-generated QBO in a forecast model was MERRA version 2 (MERRA-2; Gelaro et al. 2017), which improved the representation of QBO forcings by adopting a parameterized GWD scheme (Coy et al. 2016). While the GWD parameterization in MERRA-2 was similar to that in MERRA, the latitudinal profile of the background nonorographic GWD in the MERRA-2 was modified to include a source related to tropical and storm-track precipitation (Molod et al. 2015). The increased equatorial GWD in MERRA-2 reduced the zonal wind analysis increments compared with MERRA, thereby making the QBO mean meridional circulation more physically consistent (Coy et al. 2016). However, this GWD parameterization do not always contribute to the entire range of QBO characteristics in the equatorial stratosphere. For instance, the SAO is notably stronger at 5 hPa and above (Coy et al. 2016; Shibata and Naoe 2025). The QBO winds at 10 hPa were a clear outlier during the period before the mid-1990s, which would be attributed to the downward propagation of exceptionally strong westerly SAO phases in the reanalysis (Kawatani et al. 2016; Anstey et al. 2022a).

The second reanalysis QBO represented realistically using a self-generated QBO was the fifth generation ECMWF reanalysis (ERA5). ERA5 introduced the nonorographic GWD parametrization of the Scinocca (2003) scheme to represent the effects of upward propagating gravity waves from tropospheric sources including deep convection, frontal disturbances, and shear zones (Orr et al. 2010; Hersbach et al. 2020; Pahlavan et al. 2021a, b). The GWD parameterization in ERA5 was the same as ERA-20C, except for incorporating a latitudinal dependency of nonorographic launch flux. Using the parameterization in a free-running model run yielded a QBO-like oscillation with relatively realistic amplitudes. However, the period of these oscillations was approximately 1.2 years, which was notably shorter than the observed QBO (Orr et al. 2010).

The Japanese Reanalysis of Three Quarters of a Century (JRA-3Q) is the latest third generation of global atmospheric reanalysis spanning late 1940s onward (Kosaka et al. 2024). JRA-3Q used a scheme proposed by Scinocca (2003), which parameterized the momentum-conserving vertical propagation and dissipation processes of momentum. The dissipation processes were represented through critical-level filtering and amplitude saturation (Japan Meteorological Agency 2019). This scheme is more advanced than that in JRA-55 (S. Kobayashi et al. 2015), which only employed Rayleigh friction for layers above 50 hPa (Japan Meteorological Agency 2013).

Typical questions arise regarding the representation of the JRA-3Q QBO. How well does

JRA-3Q representation of the QBO align with other datasets? To what extent can we quantify differences in the representation of the QBO among reanalyses and observations? Is it appropriate to use reanalysis data from the pre-satellite era? Are there specific aspects of the JRA-3Q QBO that should be considered when using it? Because globally comprehensive observational datasets are not available during the pre-satellite era, the JRA-3Q QBO is evaluated by comparisons with other reanalyses and observations, as well as through comparisons between the post-satellite and pre-satellite eras. This study is conducted to evaluate the representation of JRA-3Q QBO in zonal wind and temperature, with an emphasis on maintaining consistency over time in the reanalysis QBO.

The structure of this paper is as follows. Section 2 describes the QBO in the JRA-3Q system and the methods used to isolate the QBO signal in the reanalysis. Section 3 characterizes the morphology of the QBO. In Section 4, we present results illustrating the QBO signal through the wavelet analysis, including trends in amplitude and period, as well as the latitudinal structure and longitudinal asymmetry derived from the wavelet analysis. Finally, Section 5 provides discussion and conclusions.

2. Data and Method

2.1 Datasets

Monthly mean zonal wind values, which are representative of the equatorial belt, are analyzed using data from global reanalysis datasets, including JRA-3Q, ERA5, MERRA-2, and JRA-55, along with JRA-55C (C. Kobayashi et al. 2014).

A long-term combined radiosonde dataset, compiled by the Free University of Berlin (FUB; Naujokat 1986) (https://www.geo.fu-berlin.de/en/met/ag/strat/produkte/qbo/index.html), is utilized near the equator at three stations: Canton Island (2.8°S, 171.7°W); Gan, Maldives (0.7°S, 73.1°E); and Singapore (1.4°N, 103.9°E) at the 70, 50, 40, 30, 20, 15 and 10 hPa levels from 1953 to 2020. Additional Singapore sonde data were obtained from a National Aeronautics and Space Administration (NASA) site (https://acd-ext.gsfc.nasa.gov/Data_services/met/qbo/qbo.html), covering the period from 1979 to the present. In this study, we construct a merged dataset combining the FUB data from 1953–2020 and the NASA data from 2021–2023. Hereafter, these merged data are referred to as radiosonde data (or sonde observations). For satellite observation data, we utilized temperatures measured by the Microwave Limb Sounder (MLS) instrument on the Aura satellite (AMLS), along with winds derived from the AMLS geopotential height data (Shibata and Naoe 2025). Both the AMLS temperature and geopotential height data were obtained from Level 3 monthly binned datasets, version 5.0x (Livesey et al. 2022), with a latitudinal resolution of 4.0 degrees (available online from https://acdisc.gesdisc.eosdis.nasa.gov/data/Aura_MLS_Level3/). These datasets, spanning from 2004 to 2022, are available at Aura MLS Level 3 data. The zonal wind outside the equatorial area was calculated from the geopotential height data using the gradient wind balance equation. In the vicinity of the equator, zonal wind was evaluated through cubic spline interpolation of the gradient wind outside the near-equator latitudes, following the method described by Smith et al. (2017). More detailed explanations were described by Shibata and Naoe (2025).

2.2 Wavelet analysis

The wavelet analysis provides a measure of the dominant time-dependent modes of variability by decomposing a time series in the time-frequency domain. This technique is applied to the QBO analyses (Fadnavis and Beig 2008; Naoe et al. 2017; Shibata and Naoe 2022). In this study, a Morlet mother wavelet, a plane wave modified by a Gaussian envelope, with a nondimensional frequency $\omega_0 = 6$ (e.g., Torrence and Compo 1998) is used. To examine fluctuations in the QBO power over a range of scale (or bands), the scale-averaged wavelet power P_{QBO} at a given time index is calculated. This measure represents a time series of the average variance within a specific band, derived from the weighted sum of the wavelet power spectrum within a band from 20 to 40 months. The QBO amplitude is evaluated as the square root of $2P_{QBO}$.Thus, the scale-averaged wavelet power can be used to examine the modulation of one time series by another, or the modulation of one frequency by another within the same time series.

Based on Torrence and Compo (1998), we derive the significance (or confidence level) for Fourier and wavelet spectra. A background spectrum of red noise can be modelled as a lag-1 autoregressive [AR(1)] process. The discrete Fourier power spectrum (Gilman et al. 1963) with the assumed AR(1) *α* is given by

$$P_k = \frac{1-\alpha^2}{1+\alpha^2-2\alpha\cos(2\pi k/N)}, \quad (1)$$

where $k = 1 \cdots N/2$ is the frequency index. On average, the local wavelet power spectrum is identical to the Fourier power spectrum given by Eq. (1) (Torrence and Compo 1998).

The null hypothesis for the wavelet power is defined such that if a peak in the wavelet power spectrum significantly exceeds the background spectrum, then it can be considered a true feature with a specified level of confidence (e.g., at the 95% confidence level, or equivalently significant at the 5% level). If the wavelet coefficient follows a normal distribution, then both the real and imaginary parts of the wavelet coefficient are also normally distributed. As the square of a normally distributed variable is chi-square distributed with one degree of freedom (DOF), the wavelet power spectrum should be normally distributed with two DOF, denoted by χ_2^2. Assuming a mean background spectrum of red noise as described by Eq. (1), the corresponding distribution for the local wavelet power spectrum, $|W_n(s)|^2$, is given by

$$\frac{|W_n(s)|^2}{\sigma^2} \Rightarrow \frac{1}{2} P_k \chi_2^2 \quad (2)$$

at each time *n* and wavelet scale *s*, where σ^2 is the variance and "$\Rightarrow$" indicates "is distributed as”. Thus, by selecting an appropriate AR(1), Eq. (2) can be calculated at each scale to construct 95% confidence levels.

By smoothing the wavelet spectrum in time, one can increase the DOF of each point and increase the significance of peaks in wavelet power (Appendix). Additionally, smoothing in scale increases the DOF, and thus an analytical relationship for significance levels for the scale-averaged wavelet power is described in Appendix.

The QBO amplitude is calculated by two independent methods: the direct method and the wavelet method (Shibata and Deushi 2012; Shibata and Naoe 2022). For the direct method, the QBO time series assumes a single sinusoidal wave (Pascoe et al. 2005; Baldwin and Gray 2005), for example, $A\,sin(t)$. As the peak value is *A* and the variance is $A^2/2$, the QBO amplitude is $\sqrt{2}\sigma$, where σ is the root mean square of the QBO time series over three cycles. The $\sqrt{2}$ factor is used to make the defined amplitude representative of the magnitude of the peak of the oscillation (Dunkerton and Delisi 1985). As described by Shibata and Naoe (2022), one cycle is defined as the period from one minimum point of the magnitude of the QBO time series to the second consecutive minimum point. The QBO amplitude is assigned to the center time of the three cycles. In this way, the QBO amplitudes are first calculated discretely in time, approximately half a cycle (~14 months) apart. Monthly amplitudes are then obtained through cubic interpolation using Lagrange polynomials. Henceforth, this direct method is referred to as a sigma method.

3. Representation of QBOs in Reanalyses

3.1 QBO Time Series and Spectrum

Figure 1 presents the time series of zonal-mean zonal wind at the equator for reanalysis datasets including JRA-3Q, JRA-55, ERA5 and MERRA-2, alongside observations from AMLS and radiosondes at Singapore or other near-equator stations. Overall, analyses QBOs are in good agreement with the radiosonde observations in the post-satellite era, illustrating the basic-features of the zonally-averaged QBO. The zonal winds alternate between westerly and easterly phases with variable durations. Generally, westerly QBO phases tend to persist longer at lower levels, while easterly phases dominate at higher levels. The westerly QBO phases have roughly constant amplitude with height while easterly QBO phases tend to be strengthened with increasing height (e.g., Baldwin et al. 2001; Anstey et al. 2022a). QBO disruptions, such as intrusions near 40 hPa followed by the descent of easterly anomalies within a westerly QBO phase, are evident (Newmann et al. 2016; Osprey et al. 2016; Coy et al. 2017). In the post-satellite era, the JRA-3Q QBO appears consistent with that in JRA-55. The MERRA-2 QBO winds, especially the westerly winds, appear slightly stronger, and the SAO is notably stronger at 5 hPa and above (Coy et al. 2016). Additionally, westerly onsets in MERRA-2 tend to occur earlier than westerly onsets (Anstey et al. 2022a) in the other three reanalyses.

In the pre-satellite era, deviations between the JRA-3Q QBO and radiosonde observations appear in the 1970s, showing an easterly shift in the 1960s and diminished

QBO signals in the 1950s. Meanwhile, the JRA-55 QBO during the 1960s exhibits similar characteristics to ERA5. The ERA5 QBO shows a behavior consistent with observations in the lower stratosphere dating back to the mid-1950s. The JRA-3Q QBO in its early stage exhibits a shorter period of around one year in the middle stratosphere and a diminished amplitude in the lower stratosphere before the late 1960s. Therefore, the modelled QBO in JRA-3Q has a lack of consistency with the observed QBO, and the representation of the assimilated QBO in JRA-3Q only with conventional observations is not good as that in JRA-55. It is noteworthy that while the JRA-3Q model can produce a self-generated-QBO, the atmospheric model in JRA-55 did not produce any QBO-like oscillations (Kosaka et al. 2024).

Figure 2 displays the power spectrum of zonal-mean zonal wind at the equator spanning 20 years of both post-satellite and pre-satellite eras. Three primary components are evident: a narrow spectrum of the SAO and ANN above approximately 5 hPa, with power peaks at 1 hPa and around 2 hPa, respectively, and a broad QBO spectrum between 2 and 3 years which does not overlap with the other components. For this study, QBO components are defined as oscillations with periods ranging from 20 to 40 months, consistent with previous studies (Pascoe et al. 2005; Shibata and Naoe 2022). As the QBO power peaks at approximately 20 hPa (Fig. 2), the characteristics of the QBO are primarily investigated at this altitude. The zonal wind QBO clearly dominates the wind variability in the middle stratosphere, while the temperature peaks slightly below the wind peak, with temperature variations observed above the tropical tropopause (Supplement Figure S1).

In pre-satellite era, JRA-3Q does not reproduce QBO well, exhibiting unrealistic false peaks at 9 and 18 months. Conversely, the SAO and ANN show a relatively good agreement with those in the post-satellite era. In contrast, JRA-55 effectively represents the QBO, but it does not reproduce the ANN, with its power nearly diminished and only visible around 3–5 hPa below the main ANN region. This discrepancy is likely attributed to stronger damping in the upper layers of the atmospheric model to prevent reflections from the top lid.

3.2 Comparison of processes represented by reanalysis models

Here, we describe the representation of the QBO in zonal wind and temperature in JRA-3Q compared to the JRA-55 QBO. Anstey et al. (2022a) indicated that the assimilation of satellite observations does not necessarily have a significant impact on the representation of QBO wind evolution. This finding was supported by the effective constraint of tropical radiosonde wind observations up to altitudes of 10 hPa in JRA-55, as demonstrated by the excellent agreement between JRA-55 and JRA-55C reanalyses (C. Kobayashi et al. 2014).

However, JRA-55 lacked the ability of its underlying model to self-generate its own QBO. Additionally, it included unrealistically strong damping terms in the middle atmosphere, leading to the disappearance of the ANN peak, typically observed at 2 hPa, during the pre-satellite era (Fig. 2). To mitigate the accumulation of smallest-scale noise, JRA-55 employed fourth-order linear horizontal diffusion of vorticity and divergence on spectral variables in terms of spherical harmonics (Japan Meteorological Agency 2013). These diffusion coefficients gradually increased with height in layers above 100 hPa, simulating a sponge layer designed to absorb waves approaching the upper boundary. The Rayleigh friction was also implemented for layers above 50 hPa. Vertical diffusion of momentum and heat were represented by the surface boundary layer scheme from the Level 2 turbulence closure scheme of Mellor and Yamada (1974) across the entire atmosphere (Japan Meteorological Agency 2013).

JRA-3Q improved the representation of the forecast model by adopting the more sophisticated, nonorographic GWD scheme compared to JRA-55 (Kosaka et al. 2024). The model top was extended up to 0.01 hPa from 0.1 hPa, and the vertical resolution was increased from 60 to 100 layers in JRA-3Q. To mitigate the accumulation of smallest-scale noise, second-order linear horizontal diffusion was applied to the divergence term in spherical harmonics. The diffusion coefficient progressively increased with height in a sponge layer located above 30 hPa. Vertical diffusion of momentum and heat were represented by the surface boundary layer scheme using a hybrid approach that combined a turbulence kinetic energy closure scheme based on Mellor and Yamada (1974, 1982) with an eddy diffusivity type scheme based on Han and Pan (2011) throughout the entire atmosphere (Japan Meteorological Agency 2019). As a result, the JRA-3Q is capable of reproducing ANN in the upper equatorial stratosphere during the pre-satellite era. The JRA-3Q introduced the scheme developed by Scinocca (2003), using a launch level of 450 hPa and launch momentum flux of 3.5 mPa. The Scinocca scheme is designed with simplicity;

once the properties of the launch spectrum are selected, the only tunable parameters in practice are the launch level and total launch momentum flux (Orr et al. 2010).

Here, there is a frequently faced dilemma for developers of models for operational weather prediction that lower resolution versions set up for climate simulations can be tuned to represent QBO behaviors under present day conditions that are relatively realistic (albeit imperfect) but the highest resolution versions are too expensive to run beyond the short NWP, or at most seasonal, timescales. Thus, there are double challenges: 1) How to tune the high-resolution versions of models to produce “free-running” QBOs that at least match the realism of low-resolution models given output that is overwhelmingly on short timescales heavily influenced by initial conditions. Reanalyses which cover historical periods may not have sufficient observational data to constrain the model behavior, leading to divergence between datasets prior to introduction of higher density observations. 2) How to be able to sustain QBO amplitudes further into the past with limited data availability.

Due to that dilemma that parameters representing the QBO were not sufficiently tuned, the JRA-3Q QBO exhibits a model bias when compared with observational data. In the satellite era, the model bias was corrected by the availability of sufficient satellite observations. However, in the pre-satellite era, the model bias was more pronounced due to the sparse conventional observations available in the early stage of the historical timeline. Consequently, the JRA-3Q QBO from the early 1960s and before has substantially different characteristics from the QBO observed in the post-satellite era.

4. QBO Characteristics Using the Wavelet Analysis

4.1 Wavelet spectrum and scale averaged wavelet power amplitude

Figure 3 depicts both local and global (or time-averaged) wavelet spectra of JRA-3Q zonal-mean zonal wind at 20 hPa. The local wavelet spectrum is presented for January 2010, while the time-averaged spectra span 21-years in both the post-satellite and pre-satellite eras. These spectra are normalized by a variance value of approximately 300 $m^2\ s^{-2}$. A thin gray line represents the mean red noise spectrum, which is a theoretical background noise with a AR(1) of 0.94. It is important to note that the variance and AR(1) calculations are based on deseasonalized and detrended zonal wind data exclusively from the post-satellite era, primarily from 1980 to 2022. This background spectrum serves as a reference for evaluating the QBO in the pre-satellite era as well. The upper thick gray line corresponds to the 95% confidence spectrum, assuming that the square of a normally distributed variable follows a chi-square distribution with two DOF (for each real and imaginary part of complex wavelet transform function).

Color dashed (green, red, and blue) horizontal lines represent the sum of the wavelet power spectrum between 20 and 40 months, scaled to estimate the QBO wavelet power (Torrence and Compo 1998). Thick gray horizontal dashed lines indicate the scale-averaged 95% confidence level. The scaled-averaged power associated with the QBO exceeds the 95% level during the satellite era (red line), whereas QBO power in the pre-satellite era (blue line) remains quite low and comparable to the 95% confidence level. Additionally, an unrealistic spectrum with a period of 6–12 months, which is clearly a part of model bias, is enhanced. This indicates that the representation of the JRA-3Q QBO in the early stage is significantly degraded due to the outstanding model bias and this QBO does not dominate variability in the equatorial middle stratosphere.

Figure 4 displays the time series of the wavelet power spectrum at 20 hPa for each dataset. All datasets exhibit similar behavior with amplitude peaking around 28 months within 20 to 40 months, remaining relatively constant throughout the satellite era. It appears that during the 2010s, the QBO period lengthens, displaying greater variability likely due to the QBO disruption observed in 2016 (Coy et al. 2017; Newmann et al. 2016; Osprey et al. 2016).

Figure 5 illustrates the time series of the vertical profile of wavelet power amplitude of zonal wind at the equator for the reanalyses and observations. The QBO clearly dominates the zonal wind variability in the 10–70 hPa layer, peaking around 20 hPa. It is noted that the AMLS zonal wind at the equator is evaluated using AMLS monthly geopotential height data. Therefore, the derived zonal wind serves as a rough estimation and is used qualitatively for comparison with the reanalyses. Throughout its period, including the pre-satellite era, JRA-55 QBO exhibits no significant long-term trend in the QBO amplitude, highlighting the importance of conventional observations in accurately reproducing the QBO within the JRA-55 reanalysis system (Anstey et al. 2022a). For JRA-3Q in the pre-satellite era and ERA5 in its early stage, QBO amplitudes diminish rapidly above 10 hPa falling clearly below the 95% confidence level in the post-satellite era. This suggests that no direct wind observations were assimilated at these higher altitudes in these datasets.

Figure S2 shows the time series of the vertical profile for temperature. The temperature QBO dominates variability in the 10–70 hPa layer, with amplitude ranging from 2–3 K and peaking at 20–30 hPa. Both JRA-3Q and JRA-55 exhibit variations in temperature QBO amplitudes at 5–10 hPa before and after 1998, possibly influenced by a significant transition in satellite instruments from TOVS to ATOVS suites in 1998 (Kosaka et al. 2024). Kim et al. (2019) identified systematic changes around 1998 in Kelvin wave amplitudes in JRA-55 compared with JRA-55C, suggesting impacts of different satellite data on assimilated equatorial wave fields.

QBO amplitude is calculated using both the sigma method and wavelet method for JRA-3Q. In the sigma method, one cycle is defined from the minimum points of the band-passed data, as shown by star marks in Fig. 6. Meanwhile, in the wavelet method, fluctuations are examined in power over a range of scales (or a band), and one can define the scale-averaged QBO wavelet power as the weighted sum over scales from 20 to 40 months. This scale-averaged wavelet power provides a time series of average variance within a specific band, offering insights into the modulation of frequencies within the same time series.

Figure 6 illustrates the time series of the QBO amplitude of the zonal-mean zonal wind at 20 hPa for JRA-3Q, calculated using both the sigma method and wavelet method, alongside the magnitude of band-pass filtered zonal wind. Apparently, the QBO amplitude closely tracks the envelope of the band-pass filtered zonal-mean zonal wind magnitude. The sigma method exhibits decadal variations similar to the wavelet method but with less short-period variability, indicating an effective filtering of shorter periods below a few years (Shibata and Naoe 2022). The time series reveals consistent interdecadal changes, including potential modulation in QBO variance with decadal oscillation and peaks in QBO amplitude around the late 1960s, 1983, 1995, and 2005 (Hamilton 2002; Shibata and Naoe 2022), as well as the QBO disruption observed in the late 2010s (e.g., Coy et al. 2017). The thin solid line represents the 95% confidence level for zonal wind (assuming red noise with α = 0.93), estimated from satellite era data spanning 1980–2022. Figure 7 compares the zonal wind amplitude of the JRA-3Q QBO at 20 hPa with other reanalyses, and observations from the radiosonde and AMLS. As sonde winds are sampled at specific locations, whereas the other datasets show zonally-averaged winds, the sonde amplitude of zonal wind QBO should not be considered an exact representation of the amplitude derived from reanalyses. Overall, however, almost all reanalyses show good agreement with each other and with the sonde data, and there is a marked convergence over the latest 15 years. In the 1982–2020 average, the QBO amplitude for the mean of the four reanalyses is 22.8 m s^{-1}, slightly lower than the sonde amplitude of 25.0 m s^{-1}.In contrast, the AMLS QBO amplitude during 2007–2020 underestimates the four reanalysis mean by 22%, although this value exceeds the 95% confidence level of the 4-reanalysis mean. Specifically, the JRA-3Q QBO amplitude during the satellite era appears as somewhat of an outlier before the mid-2000s, reduced by 8% compared with the other reanalyses.

In the pre-satellite era, the JRA-3Q QBO amplitude significantly deteriorates falling below the 95% level in the early 1960s and before. The ERA5 QBO amplitude (and JRA-55 QBO amplitude) exhibit behavior consistent with sonde observations, remaining above the 95% confidence level as long as conventional sonde observational data are available. Prior to the availability of radiosonde data, however, the ERA5 QBO amplitude also falls below the 95% level.

Anstey et al. (2022a) suggested that differences in QBO representation between JRA-55 and JRA-55C did not exhibit any long-term trend, indicating that the increasing incorporation of satellite data into JRA-55 did not significantly improve QBO representation compared to conventional observations alone. In the JRA-3Q data assimilation system, the nonorographic GWD scheme was used for improving the representation of the QBO. These results suggest that satellite data are important for correcting significant model biases in the JRA-3Q data assimilation system. While the GWD scheme in JRA-3Q is beneficial, it does not inherently guarantee the generation of a realistic QBO, particularly evident in the pre-satellite era.

Comparing the zonal wind QBO to the temperature QBO, it is expected that the inter-reanalysis spread of zonal wind is larger in the tropics than that of temperature due to the weaker constraint provided by satellite-derived temperature observations. In Fig. 7b, it is evident that the temperature QBO from AMLS shows a good agreement with those from the reanalyses. The temperature QBOs exhibit amplitudes of 2–3 K at 30 hPa, with a mean value of 2.3 K for the 5-dataset mean (4 reanalysis plus AMLS) in the satellite era, which exceeds the 95% confidence level for the 5-dataset mean. The difference in temperature QBO amplitude between JRA-55 and ERA5 is relatively small during the satellite era and the 1970s. The temperature QBO amplitude for JRA-3Q is deviated from JRA-55 or ERA5 in the 1960s and earlier.

4.2 Trends of the QBO amplitude and period

As we saw some increasing tendency of QBO periods in the 2010s, we conduct the trend analysis during the post-satellite era. Figure 8 presents the time series of QBO periods and amplitudes for zonal wind at 20 hPa and temperature at 10 hPa, using JRA-3Q and other datasets. Linear regression lines are plotted for the period from 1982 to 2020 to mitigate edge effects in the wavelet analysis data from the post-satellite era.

The period of the zonal wind QBO at 20 hPa ranges from 24 to 36 months in both JRA-3Q and radiosonde data. There seems decadal variation, or there are clusters of shorter and longer periods. A linear regression indicates less than 1 mon de^{-1} with no confidence, suggesting that this may just be an artifact of random variability. For the QBO amplitude, JRA-3Q shows a flattened trend while the radiosonde exhibits a decreasing trend. The temperature QBO exhibits similar behavior to the zonal wind QBO.

Figure 9 depicts the vertical profile of QBO amplitude trends and peak-period trends for the reanalyses and observational data during the satellite era. To assess the statistical significance of trends, an effective, decorrelation time for the QBO is assumed to be 14 months. Overall, trends of QBO periods and amplitudes have lack of confidence. There is confidence in the upper stratosphere for both the QBO amplitude and period although this does appear to target less important situations where the QBO amplitudes are starting to drop off and the signal is ceasing to dominate SAO and AAN. In the middle-to-lower stratosphere, many datasets exhibit decreasing trends of QBO amplitude without the statistical significance. The QBO periods of the power peaks of zonal wind and temperature exhibit consistent pattern from the lower-to-middle stratosphere, and this similarity comes from the fact that the radiosonde dataset is largely constraining the reanalyses.

The QBO phase transition exhibits quasi-decadal variations, occasionally synchronizing with the seasonal cycle (Hampson and Haynes 2004; Read and Castrejón-Pita 2012; Anstey and Shepherd 2014). Figure 10 illustrates the time series of the seasonal march of zonal-mean zonal wind at 20 hPa. To visualize the QBO phase transitions and their alignment with the annual cycle, the x-axis represents a 2-year interval (i.e., 25 months) and the y-axis displays data every two years. During the satellite era, the QBOs exhibit strikingly similar characteristics in terms of periods, amplitude, phase transition between westerlies and easterlies across various reanalyses, including JRA-55C. Notably, JRA-3Q shows smaller easterly anomalies compared with JRA-55 and ERA5. In this figure, there are periods in

1970s and 1980s where the phase angle drifts at approximately a fixed rate with respect to the annual cycle, whereas the 1990s and 2000s show seasonal synchronization, corresponding to times with little or no drift (Anstey and Shepherd 2014). However, the previous figure of the trend analysis indicated that at the 20–30 hPa levels, the peak-period of the QBO exhibits an increasing trend. This apparent trend of the QBO period can be primarily attributed to the stagnation of the QBO phase transition in the 2010s, potentially influenced by the QBO disruption in 2016.

4.3 Latitudinal and longitudinal variations of the QBO amplitude

Figure 11 depicts the latitudinal distribution of the QBO amplitude in zonal wind and temperature for the reanalyses and AMLS during the satellite era. Gray lines in Figs. 11b and 11d represent the 95% confidence level in smoothing in time and scale against the red noise background field averaged over the four reanalyses. It is noted that the smoothing procedure increase the DOF, thereby enhancing confidence in regions of significant power. The zonal wind QBO peaks in the mid-stratosphere with a half-width of 12°–13° in latitude (Fig. 11a, b), whereas the temperature peak occurs slightly below the wind peak with a narrower half-width of approximately 10° (Figs. 11c, d). The temperature peak is linked to the vertical shear of the zonal wind below the descending QBO phase. The temperature anomaly extends into the subtropics, with clear subtropical lobes in the temperature amplitude at 5 hPa down to 50 hPa in the Northern Hemisphere, though they are much less pronounced in the Southern Hemisphere, indicative of the QBO mean meridional circulation (Plumb and Bell 1982). Overall, the latitudinal structure remains consistent across the reanalyses. However, the JRA-3Q QBO amplitude is reduced by 10% and 3%–4% for zonal wind and temperature, respectively, compared with the other reanalyses. This amplitude reduction was probably caused by stronger vertical diffusion and stronger nonorographic GWD flux.

The longitudinal distribution of QBO amplitude at the equator is further examined in Fig. 12, which presents a longitude-height cross section of the zonal wind QBO amplitude and its anomaly from the zonal mean. At higher altitudes, a wave-1 structure with positive and negative amplitude anomalies, approximately 1 m s^{-1} in magnitude, dominates the Eastern and Western Hemispheres, respectively, with a westward tilt with height in the lower-to-middle stratosphere. In the lowermost stratosphere, larger amplitudes of the zonal wind QBO are observed over the central Pacific with anomaly magnitude reaching up to 1 m s^{-1}, while amplitudes in the Western Hemisphere are smaller. Overall, the characteristics of zonal wind QBO amplitude in the longitude-height section are consistent across the reanalyses.

The meridional propagation of the extratropical quasi-stationary wave in the winter Hemisphere leads to zonal asymmetry of the QBO amplitude in the middle stratosphere (Hamilton et al. 2004). More specifically, this zonal asymmetry can be partly attributable to the mode structures of quasi-stationary equatorial Rossby and Kelvin waves during strong westerly and easterly phase of the QBO (Sakazaki and Hamilton 2022). In the lower stratosphere the zonal asymmetries may reflect the upward extension of the tropospheric Walker circulation (Hamilton et al. 2004).

Figure 13 illustrates the longitudinal distribution of temperature QBO amplitude and its anomalies from the zonal mean at the equator. In the middle stratosphere, the temperature QBO has an amplitude of 1–2 K, and a wave-1 structure with negative and positive anomalies of approximately 0.1 K in the Eastern and Western Hemispheres, respectively, is evident across the reanalyses. In the lower stratosphere, smaller-scale anomalies are present with a local maximum over Indonesia as identified in a previous study (Tegtmeier et al. 2020). However, the detailed structures differ among the reanalyses. Zonal asymmetries are prominent in the temperature signal, with the QBO amplitude in the Indonesian region being approximately 10%–20% larger than the zonal-mean amplitude. This result is attributed to Kelvin wave variability near the equatorial tropopause, which modulates the climatological cold tropopause over Indonesia. Enhanced wave amplitudes coincide with the descending phase of the QBO-W (Randel and Wu, 2005).

The most distinct characteristics observed are the apparent disconnection of the temperature QBO anomalies between the lower and middle stratosphere in JRA-55, ERA5, and MERRA-2. The amplitude anomalies of JRA-3Q temperature QBO exhibit an eastward tilt with height in the lower-to-middle stratosphere. Clear positive anomalies around 120°E at 20–30 hPa are found in ERA5 and MERRA-2, whereas a less pronounced anomaly is seen in JRA-55. The underlying reasons for these anomalies are currently unknown. One possible explanation is that, although the assimilation of satellite observations does not significantly impact the representation of the QBO wind evolution, inconsistency may arise in the temperature field due to the data assimilation process. This involves combining radiosonde winds and satellite radiance data, with the vertical weighting function associated with different channels of nadir-sounding instruments potentially contributing these anomalies. Anther possible explanation is that ozone distribution (input or modelled) that is used for radiative process in the forecast model might differ from reality. Further studies are needed to explore the consistency and impacts of the radiosonde winds on the data assimilation system.

5. Discussion and Conclusion

We evaluated the representation of the JRA-3Q QBO in zonal wind and temperature, with a focus on its temporal consistency during both the post- and pre-satellite eras. To achieve this, we compared the low-frequency variability and trends in the JRA-3Q QBO during the post-satellite era with those from other reanalyses, including JRA-55, -55C, ERA5, and MERRA2, as well as observational datasets. Owing to the lack of global coverage in observational datasets during the pre-satellite era, the JRA-3Q QBO was also compared with other reanalyses and analyzed between the post- and pre-satellite eras. A novel feature of the validation methods employed is the quantification of the extent of disagreement between the post- and pre-satellite eras, derived from the red noise background spectrum based on the post-satellite era.

Here we answer several questions regarding the representation of the JRA-3Q QBO raised in Introduction. 1) How well does JRA-3Q representation of the QBO align with other datasets? As described in Section 3.2, the introduction of the nonorographic GWD contributed to improving the representation of the QBO in reanalyses to some extent. The forecast models in the latest reanalyses resolved the stratosphere to exhibit an observed-QBO-like oscillation in zonal-mean zonal wind. Overall, almost all reanalyses showed good agreement with each other and with the sonde data, and there is a marked convergence over latest 15 years (from the late 2010s to onward).

2) To what extent can we quantify differences in the representation of the QBO among

reanalyses and observations? The JRA-3Q QBOs in zonal wind and temperature during the satellite era were slightly reduced compared with other reanalyses such as JRA-55, ERA5, and MERRA-2. Specifically, the QBO amplitudes at 20–30 hPa in JRA-3Q were reduced by 8% and 4%, respectively, compared with the other reanalyses. The QBO periods of the power peaks were coincident across the reanalyses in the lower-to-middle stratosphere owing to the radiosonde dataset largely constraining the reanalyses. QBO amplitudes seem have decreasing trends in the middle-to-lower stratosphere and the QBOs in the 20–30 hPa layers exhibit longer periods although most trends of QBO periods and amplitudes have lack of confidence.

3) Is it appropriate to use reanalysis data from the pre-satellite era? We quantified the disagreement between the post- and pre-satellite eras using the red noise background spectrum based on the post-satellite era data. The QBO periods of the power peaks showed an agreement with each other in the lower-to-middle stratosphere. However, the JRA-3Q QBO from the early 1960s and before is substantially degraded, falling below the 95% confidence level. In contrast, there was an improvement in the representation of the JRA-3Q ANN in the equatorial stratosphere, whereas the JRA-55 ANN in the pre-satellite era completely disappeared due to unrealistically strong damping in the model's upper layers.

4) Are there specific aspects of the JRA-3Q QBO that should be considered when using it? Overall, the latitudinal structure is consistent among the reanalyses, with the exception of the amplitude in JRA-3Q. The zonal asymmetry of the zonal wind QBO amplitude is

dominated by a wave-1 structure with a magnitude of about 1 m s^{-1} in the middle-to-upper stratosphere. Larger amplitudes of the zonal wind QBO are observed over the central Pacific, while smaller amplitudes are present in the Western Hemisphere, with magnitudes up to 1 m s^{-1}, in agreement with previous studies. In the lowermost stratosphere, smaller-scale anomalies of the temperature QBO amplitude with a local maximum over Indonesia are evident, as identified in previous studies. However, the detailed structures of these anomalies differ among the reanalyses. One of the most distinct characteristics of these zonal asymmetries is the disconnection of the temperature QBO anomalies between the lower and middle stratosphere in JRA-55, ERA5 and MERRA-2. Additionally, the amplitude anomalies of the JRA-3Q temperature QBO exhibit an eastward tilt with height in the lower-to-middle stratosphere. The underlying reasons for these anomalies are currently unknown. Possible explanations are that data assimilation between radiosonde winds and satellite radiance may introduce inconsistencies in the temperature field or that input or modelled ozone distribution might be different from reality.

In conclusion, the forecast models in the latest reanalyses presented in this paper still exhibit numerous biases, indicating that further improvements are needed to enhance their representation for more accurate diagnostics. Critical deficiencies in QBO-resolving models include inaccuracies in the mean QBO period and amplitude, the latitudinal width, especially latitudinal and vertical extents in the lower stratosphere, the vertical width, and other related factors (Bushell et al. 2020; Schenzinger et al. 2017). Improving these factors, especially in a pre-satellite era, is particularly important for capturing tropical variability in the stratosphere and QBO teleconnections within both extratropical circulation and the tropical troposphere.

The double challenging issues raised in Section 3.2 would have a broader applicability than simply development of reanalysis systems, and understanding their limitations, due to the recent explosion of machine learning activity for meteorology and its reliance on reanalysis data for training and testing. There are clear implications for anyone seeking to use reanalyses in this context for QBO prediction if the data covers an era when reanalyses show divergent behavior. There are also implications for those attempting to avoid dependence on reanalysis products by ingesting observations directly if this does not guarantee realistic QBO properties.

Finally, state-of-the-art current data assimilation systems are characterized by background error covariances with shorter horizontal correlation lengths compared to their predecessor (Kosaka et al. 2024). Artificial changes can arise due to variations in the quality and quantity of input observational data, especially before and after satellite data, after the introduction of the AMSU satellite observations around 1998, and the absence of tropical radiosonde data. Therefore, next-generation reanalysis projects will adopt or implement appropriate background error-correlation lengths over the course of time, especially during significant discontinuities in the input observational data.

Appendix

Following Torrence and Compo (1998), this Appendix describes the statistical significance tests for wavelet spectrum.

a. Wavelet transform

Consider a time series of signal, x_n, with equal time spacing δt and the time index *n* = 0 … *N* − 1. The wavelet transform, $W_n(s)$, is defined as the convolution of x_n with the wavelet scale *s*. By the convolution theorem, the wavelet transform is expected using the wavelet function ψ:

$$W_n(s) = \sum_{k=0}^{N-1} x_k \psi^*(s\omega_k) \mathrm{e}^{i\omega_k n\,\delta t}, \qquad \text{(a1)}$$

where *k* = 0 … *N* − 1 is the frequency index, ω_k is the angular frequency, and (*) denotes the complex conjugate.

The total energy is conserved in the wavelet transform, and the equivalent *Parseval's theorem* for wavelet analysis is given by:

$$\sigma^2 = \frac{\delta j\ \delta t}{C_\delta\ N} \sum_{n=0}^{N-1} \sum_{j=0}^{J} \frac{|W_n(s_j)|^2}{s_j}, \qquad \text{(a2)}$$

where σ denotes the variance, *j* represents the wavelet scale index, and $\delta j = 0.125$, C_δ $= 0.776$.

b. Smoothing in time and scale

The time-averaged wavelet spectrum over a certain period is defined as

$$W_n^2(s) = \frac{1}{n_a}\sum_{n_1}^{n_2} |W_n(s)|^2, \qquad \text{(a3)}$$

where $n_a = n_2 - n_1 + 1$ denotes the number of points averaged over. The time-averaged confidence level is best described by the distribution $P_k \chi_v^2 / \nu$, where P_k is the original assumed background spectrum, and χ_v^2 follows a chi-square distribution with ν DOF:

$$\nu = 2\sqrt{1 + f_T{}^2},\ f_T = \frac{n_a \delta t}{\gamma s}, \qquad \text{(a4)}$$

where n_a represents number of points averaged over, δt denotes the time step, and $\gamma = 2.32$.

The scale-averaged wavelet power can be defined as the weighted sum of the wavelet power spectrum over scales s_1 to s_2:

$$\overline{W_n}^2 = \frac{\delta j\ \delta t}{C_\delta} \sum_{j_1}^{j_2} \frac{|W_n(s_j)|^2}{s_j}. \quad \text{(a5)}$$

where $\delta j = 0.125$, $\delta j_0 = 0.6$. The DOF ν for the scale-averaged wavelet power spectrum can be modeled as

$$\nu = \frac{2 n_b S_{avg}}{S_{mid}} \sqrt{1 + f_S{}^2},\ f_S = \frac{n_a \delta j}{\delta j_0}, \quad \text{(a6)}$$

where n_b represents the number of scales averaged over, $S_{mid} = s_2\ 2^{(j_1 + j_2) d_j / 2}$, and S_{avg} is defined as

$$S_{avg} = \left(\sum_{j=j_1}^{j_2} \frac{1}{s_j} \right)^{-1}. \qquad \text{(a7)}$$

Similarly, the DOF ν for the time-and-scale-averaged wavelet power spectrum can be modeled as

$$\nu = \frac{2 n_b S_{avg}}{S_{mid}} \sqrt{1 + f_S{}^2} \sqrt{1 + f_T{}^2}\ \sqrt[4]{1 + f_S f_T}. \qquad \text{(a8)}$$

Data Availability Statement

The JRA-3Q and JRA-55 reanalysis data are accessible through collaborative organizations listed in the JRA website (https://jra.kishou.go.jp). The ERA5 reanalysis data can be obtained from the ECMWF website (https://www.ecmwf.int/en/forecasts/datasets/browse-reanalysis-datasets). Similarly, the MERRA-2 reanalysis data can be obtained from the NASA website (https://disc.gsfc.nasa.gov/datasets/).

Monthly temperature and geopotential height data from the MLS instrument can be obtained from the NASA website (https://acdisc.gesdisc.eosdis.nasa.gov/data/Aura_MLS_Level3/).

Supplement

Supplement 1 represents the power spectra of zonal-mean temperature (Figure S1).

Supplement 2 displays the time series of profile of wavelet power amplitude of temperature (Figure S2).

Acknowledgments

The authors would like to thank Takafumi Kanehama for his helpful advices on representation of QBO in JMA forecast models. HN was partly supported by the Japan Society for the Promotion of Science KAKENHI (grant numbers: JP18K03748, JP20H05171, JP22H04493, JP24K07140, JP24K00710).

References

Anstey, J.A., L.J. Gray, M. Fujiwara, I. Ivanciu, Y. Kawatani, G. Kiladis, Y.-H. Kim, P. Martineau, V. Schenzinger, S. Tegtmeier, and C. Wright, 2022a: Chapter 9: Quasi-Biennial Oscillation, in SPARC Reanalysis Intercomparison Project (S-RIP) Final Report. Fujiwara, M., G. L., Manney, L. J. Gray, and J. S. Wright (Eds.), SPARC Report No. 10, WCRP-6/2021, 612pp. doi: 10.17874/800dee57d13. [Available online at https://www.sparc-climate.org/sparc-report-no-10/, accessed 13 June 2022]

Anstey, J. A., S. M. Osprey, J. Alexander, M. P. Baldwin, N. Butchart, L. Gray, Y. Kawatani, and J. H. Richter, 2022b: Impacts, processes and projections of the quasi-biennial oscillation. *Nat. Rev. Earth Environ*., **3**, 588–603.

Anstey, J. A. and T. G. Shepherd, 2014: High-latitude influence of the quasi-biennial oscillation. *Quart. J. Roy. Meteor. Soc*., **140**, 1–21.

Baldwin, M. P., L. J. Gray, T. J. Dunkerton, K. Hamilton, P. H. Haynes, W. J. Randel, J. R. Holton, M. J. Alexander, I. Hirota, T. Horinouchi, D. B. A. Jones, J. S. Kinnersley, C. Marquardt, K. Sato, and M. Takahashi, 2001: The quasi-biennial oscillation. *Rev. Geophys*., **39**, 179–229.

Baldwin, M. P., and L. J. Gray, 2005: Tropical stratospheric zonal winds in ECMWF ERA-40 reanalysis, rocketsonde data, and rawinsonde data. *Geophys. Res. Lett*., **32**, L09806, doi:10.1029/2004GL022328.

Bushell, A.C., J.A. Anstey, N. Butchart, Y. Kawatani, S.M. Osprey, J.H. Richter, F. Serva, P. Braesicke, C. Cagnazzo, C.-C. Chen, H.-Y. Chun, R.R. Garcia, L.J. Gray, K. Hamilton, T. Kerzenmacher, Y.-H. Kim, F. Lott, C. McLandress, H. Naoe, J. Scinocca, A.K. Smith, T.N. Stockdale, S. Versick, S. Watanabe, K. Yoshida, S. Yukimoto, 2022: Evaluation of the Quasi-Biennial Oscillation in global climate models for the SPARC QBO-initiative. *Q. J. R. Meteorol. Soc.*, **148**, 1459–1489.

Butchart, N., J.A. Anstey, K. Hamilton, S. Osprey, C. McLandress, A.C. Bushell, Y. Kawatani, Y.-H. Kim, F. Lott, J. Scinocca, T. Stockdale, O. Bellprat, P. Braesicke, C. Cagnazzo, C.-C. Chen, H.-Y. Chun, M. Dobrynin, R.R. Garcia, J. Garcia-Serrano, L.J. Gray, L. Holt, T. Kerzenmacher, H. Naoe, H. Pohlmann, J.H. Richter, A.A. Scaife, V. Schenzinger, F. Serva, S. Versick, S. Watanabe, K. Yoshida, and S. Yukimoto, 2018: Overview of experiment design and comparison of models participating in phase 1 of the SPARC Quasi-Biennial Oscillation initiative (QBOi). *Geosci. Model Dev.*, **11**, 1009–1032.

Coy, L., K. Wargan, A. M. Molod, W. R. McCarty, and S. Pawson, 2016: Structure and dynamics of the quasi-biennial oscillation in MERRA-2. *J. Clim.*, **29**, 5339–5354.

Coy, L., P. A. Newman, S. Pawson, and L. R. Lait, 2017: Dynamics of the disrupted 2015/16 quasi-biennial oscillation. *J. Clim.*, **30**, 5661–5674.

Dunkerton, T. J. and D. P. Delisi, 1985: Climatology of the equatorial lower stratosphere. *J. Atmos. Sci.*, **42**, 376–396.

Ern, M., M. Diallo, P. Preusse, M. G. Mlynczak, M. J. Schwartz, Q. Wu, and M. Riese, 2021: The semiannual oscillation (SAO) in the tropical middle atmosphere and its gravity wave driving in reanalyses and satellite observations. *Atmos. Chem. Phys.*, **21**, 13763–13795.

Fadnavis, S., and G. Beig, 2008: Spatiotemporal variation of the ozone QBO in MLS data by wavelet analysis. *Ann. Geophys.*, **26**, 3719–3730.

Gelaro, R., W. McCarty, M. J. Suárez, R. Todling, A. Molod, L. Takacs, C. A. Randles, A. Darmenov, M. G. Bosilovich, R. Reichle, K. Wargan, L. Coy, R. Cullather, C. Draper, S. Akella, V. Buchard, A. Conaty, A. M. da Silva, W. Gu, G. Kim, R. Koster, R. Lucchesi, D. Merkova, J. E. Nielsen, G. Partyka, S. Pawson, W. Putman, M. Rienecker, S. D. Schubert, M. Sienkiewicz, and B. Zhao, 2017: The Modern-Era Retrospective Analysis for Research and Applications, Version 2 (MERRA-2). *J. Clim.*, **30**, 5419–5454.

Gilman, D. L., F. J. Fuglister, and J. M. Mitchell Jr., 1963: On the power spectrum of "red noise". *J. Atmos. Sci.*, **20**, 182–184.

Giorgetta, M. A., E. Manzini, and E. Roeckner, 2002: Forcing of the quasi-biennial oscillation from a broad spectrum of atmospheric waves. *Geophys. Res. Lett.*, **29**, 1245, doi:10.1029/2002GL014756.

Global Modeling and Assimilation Office (GMAO) (2015), MERRA-2 instM_3d_ana_Np: 3d,Monthly mean,Instantaneous,Pressure-Level,Analysis,Analyzed Meteorological Fields V5.12.4, Greenbelt, MD, USA, Goddard Earth Sciences Data and Information Services Center (GES DISC), Accessed: [2024/05/24], 10.5067/V92O8XZ30XBI

Hamilton, K., R. J. Wilson, and R. S. Hemler, 1999: Middle atmosphere simulated with high vertical and horizontal resolution versions of a GCM: Improvements in the cold pole bias and generation of a QBO-like oscillation in the tropics. *J. Atmos. Sci*., **56**, 3829–3846.

Hamilton, K., 2002: On the quasi-decadal modulation of the stratospheric QBO period. *J. Clim.*, **15**, 2562–2565.

Hamilton, K., A. Hertzog, F. Vial, and G. Stenchikov, 2004: Longitudinal variation of the stratospheric quasi-biennial oscillation. *J. Atmos. Sci*., **61**, 383–402.

Hampson, J. and P. Haynes, 2004: Phase Alignment of the Tropical Stratospheric QBO in the Annual Cycle. *J. Atmos. Sci*., **61**, 2627–2637.

Han, J. and H.-L. Pan, 2011: Revision of convection and vertical diffusion cchemes in the NCEP global forecast system. *Weather and Forecasting*, **26**, 520–533.

Hersbach, H., B. Bell, P. Berrisford, S. Hirahara, A Horányi, J. Munoz-Sabater, J. Nicolas, C. Peubey, R. Radu, D. Schepers, A. Simmons, C. Soci, S. Abdalla, X. Abellan, G. Balsamo, P. Bechtold, G. Biavati, J. Bidlot, M. Bonavita, G. De Chiara, P. Dahlgren, D. Dee, M. Diamantakis, R. Dragani, J. Flemming, R. Forbes, M. Fuentes, A. Geer, L. Haimberger, S. Healy, R. J. Hogan, E. Hólm, M. Janisková, S. Keeley, P. Laloyaux, P. Lopez, C. Lupu, G. Radnoti, P. de Rosnay, I. Rozum, F. Vamborg, S. Villaume, and J.-N. Thépaut, 2020: The ERA5 global reanalysis. *Quart. J. Roy. Meteor. Soc*., **146**, 1999–2049.

Hines, C. O., 1997: Doppler-spread parameterization of gravity-wave momentum deposition in the middle atmosphere. 2. Broad and quasi monochromatic spectra, and implementation. *J. Atmos. Sol. Terr. Phys.*, **59**, 387–400.

Japan Meteorological Agency, 2013: Outline of the operational numerical weather prediction at the Japan Meteorological Agency. Appendix to WMO Technical Progress Report on the Global Data-processing and Forecasting System (GDPFS) and Numerical Weather Prediction (NWP) Research, JMA, Japan, 188pp. https://www.jma.go.jp/jma/jma-eng/jma-center/nwp/nwp-top.htm

Japan Meteorological Agency, 2019: Outline of the operational numerical weather prediction at the Japan Meteorological Agency. Appendix to WMO Technical Progress Report on the Global Data-processing and Forecasting System (GDPFS) and Numerical Weather Prediction (NWP) Research, JMA, Japan, 229pp, https://www.jma.go.jp/jma/jma-eng/jma-center/nwp/nwp-top.htm.

Kawatani, Y., K. Hamilton, K. Miyazaki, M. Fujiwara, and J. A. Anstey, 2016: Representation of the tropical stratospheric zonal wind in global atmospheric reanalyses. *Atmos. Chem. Phys.*, **16**, 6681–6699.

Kim, Y.-H., G. N. Kiladis, J. R. Albers, J. Dias, M. Fujiwara, J. A. Anstey, I.-S. Song, C. J. Wright, Y. Kawatani, F. Lott, and C. Yoo., 2019: Comparison of equatorial wave activity in the tropical tropopause layer and stratosphere represented in reanalyses. *Atmos. Chem. Phys.*, **19**, 10027–10050.

Kobayashi, C., H. Endo, Y. Ota, S. Kobayashi, H. Onoda, Y. Harada, K. Onogi, and H. Kamahori, 2014: Preliminary results of the JRA-55C, an atmospheric reanalysis assimilating conventional observations only. *SOLA*, **10**, 78–82.

Kobayashi, S., Y. Ota, Y. Harada, A. Ebita, M. Moriya, H. Onoda, K. Onogi, H. Kamahori, C. Kobayashi, H. Endo, K. Miyaoka, and K. Takahashi, 2015: The JRA-55 reanalysis: General specifications and basic characteristics. *J. Meteor. Soc. Japan*, **93**, 5–48.

Kosaka Y., S. Kobayashi, Y. Harada, C. Kobayashi, H. Naoe, K. Yoshimoto, M. Harada, N. Goto, J. Chiba, K. Miyaoka, R. Sekiguchi, M. Deushi, H. Kamahori, T. Nakaegawa, T. Y. Tanaka, T. Tokuhiro, Y. Sato, Y. Matsushita, and K. Onogi, 2024: The JRA-3Q reanalysis. *J. Meteor. Soc. Japan*, **102**, 49–109.

Livesey N. J., W. G. Read, P. A. Wagner, L. Froidevaux, M. L. Santee, M. J. Schwartz, A. Lambert, L. F. M. Valle, H. C. Pumphrey, G. L. Manney, R. A. Fuller, R. F. Jarnot, B. W. Knosp, R. R. Lay, 2022: Aura Microwave Limb Sounder (MLS) version 5.0x level 2 and 3 data quality and description document. *JPL*, D-105336 Rev. B, https://mls.jpl.nasa.gov/data/v5-0_data_quality_document.pdf.

McLandress, C. and J. F. Scinocca, 2005: The GCM response to current parameterizations ofnonorographic gravity wave drag. *J. Atmos. Sci.*, **62**, 2394–2413.

Mellor, G. L. and T. Yamada, 1974: A hierarchy of turbulence closure models for planetary boundary layers. *J. Atmos. Sci.*, **31**, 1791–1806.

Mellor, G. L. and T. Yamada, 1982: Development of a turbulence closure model for geophysical fluid problems. *Rev. Geophys. Space Phys.*, **20**, 851–875.

Molod, A., L. Takacs, M. Suarez, and J. Bacmeister, 2015: Development of the GEOS-5 atmospheric general circulation model: Evolution from MERRA to MERRA2. *Geosci. Model Dev.*, **8**, 1339–1356.

Naoe, H., M. Deushi, K. Yoshida, and K. Shibata, 2017: Future changes in the ozone quasi-biennial oscillation with increasing GHGs and ozone recovery in CCMI simulations. *J. Clim.*, **30**, 6977–6997.

Naujokat, B., 1986: An update of the observed quasi-biennial oscillation of the stratospheric winds over the tropics. *J. Atmos. Sci.*, **43**, 1873–1877.

Newman, P. A., L. Coy, S. Pawson, and L. R. Lait, 2016: The anomalous change in the QBO in 2015-2016. *Geophys. Res. Lett.*, **43**, 8791–8797.

Orr, A., P. Bechtold, J. Scinocca, M. Ern, and M. Janiskova, 2010: Improved middle atmosphere climate and forecasts in the ECMWF model through a nonorographic gravity wave drag parameterization. *J. Clim.*, **23**, 5905–5926.

Osprey, S. M., N. Butchart, J. R. Knight, A. A. Scaife, K. Hamilton, J. A. Anstey, V. Schenzinger, C. Zhang, 2016: An unexpected disruption of the atmospheric quasi-biennial oscillation. *Science*, **353**, 1424–1427.

Pahlavan, H. A., Q. Fu, J. M. Wallace, and G. N. Kiladis, 2021a: Revisiting the quasi-biennial oscillation as seen in ERA5. Part I: description and momentum budget. *J. Atmos. Sci.*, **78**, 673–691.

Pahlavan, H. A., J. M. Wallace, Q. Fu, and G. N. Kiladis, 2021b: Revisiting the quasi-biennial oscillation as seen in ERA5. Part II: Evaluation of waves and wave forcing. *J. Atmos. Sci.*,

78, 693–707.

Pascoe, C. L., L. J. Gray, S. A. Crooks, M. N. Juckes, and M. P. Baldwin, 2005: The quasi-biennial oscillation: Analysis using ERA-40 data. *J. Geophys. Res.*, **110**, D08105, doi:10.1029/2004JD004941.

Poli, P., H. Hersbach, D. P. Dee, P. Berrisford, A. J. Simmons, F. Vitart, P. Laloyaux, D. G. H. Tan, C. Peubey, J.-N. Thepaut, Y. Tremolet, E. V. Holm, M. Bonavita, L. Isaksen, and M. Fisher, 2016: ERA-20C: An atmospheric reanalysis of the 20th century. *J. Clim.*, **29**, 4083–4097.

Polichtchouk, I., R. Hogan, T. G. Shepherd, P Bechtold, T. Stockdale, S. Malardel, S.-J. Lock, L. Magnusson, 2017: What influences the middle atmosphere circulation in the IFS? *ECMWF Technical Memoranda*, **809**.

Plumb, R. A. and R. C. Bell, 1982: A model of the quasi-biennial oscillation on an equatorial beta-plane. *Quart. J. Roy. Meteor. Soc.*, **108**, 335–352.

Randel, W., P. Udelhofen, E. Fleming, M. Geller, M. Gelman, K. Hamilton, D. Karoly, D. Ortland, S. Pawson, R. Swinbank, F. Wu, M. Baldwin, M.-L. Chanin, P. Keckhut, K. Labitzke, E. Remsberg, A. Simmons, and D. Wu, 2004: The SPARC intercomparison of middle atmosphere climatologies. *J. Clim.*, **17**, 986–1003.

Randel, W. J., and F. Wu, 2005: Kelvin wave variability near the equatorial tropopause observed in GPS radio occultation measurements. *J. Geophys. Res.*, **110**, D03102, doi:10.1029/2004JD005006.

Read, P. L., A. A. Castrejón-Pita, 2012: Phase synchronization between stratospheric and tropospheric quasi-biennial and semi-annual oscillations. *Q. J. R. Meteorol. Soc.*,**138**, 1338–1349.

Rienecker, M. M., M. J. Suarez, R. Gelaro, R. Todling, J. Bacmeister, E. Liu, M. G. Bosilovich, S. D. Schubert, L. Takacs, G.-K. Kim, S. Bloom, J. Chen, D. Collins, A. Conaty, A. da Silva, W. Gu, J. Joiner, R. D. Koster, R. Lucchesi, A. Molod, T. Owens, S. Pawson, P. Pegion, C. R. Redder, R. Reichle, F. R. Robertson, A. G. Ruddick, M. Sienkiewicz, and J. Woollen, 2011: MERRA: NASA's modern-era retrospective analysis for research and applications. *J. Clim*, **24**, 3624–3648.

Saha, S., S. Moorthi, X. Wu, J. Wang, S. Nadiga, P. Tripp, D. Behringer, Y.-T. Hou, H.-y. Chuang, M. Iredell, M. Ek, J. Meng, R. Yang, M. P. Mendez, H. v. d. Dool, Q. Zhang, W. Wang, M. Chen, and E. Becker, 2014: The NCEP climate forecast system version 2. *J. Clim.*, **27**, 2185–2208.

Sakazaki, T., and K. Hamilton, 2022. Discovery of quasi-stationary equatorial waves trapped in stratospheric QBO westerly and easterly jets. *J. Geophys. Res.*, **12**7, e2021JD035670. https://doi.org/10.1029/2021JD035670

Scaife, A. A., N. Butchart, C. D. Warner, D. Stainforth, W. Norton, and J. Austin, 2000: Realistic quasi-biennial oscillations in a simulation of the global climate. *Geophys. Res. Lett.*, **27**, 3481–3484.

Scinocca, J. F., 2003: An accurate spectral nonorographic gravity wave drag parameterization for general circulation models. *J. Atmos. Sci.*, **60**, 667–682.

Schenzinger, V., S. Osprey, L. Gray, and N. Butchart, 2017: Defining metrics of the quasi-biennial oscillation in global climate models. *Geosc. Mod. Dev.*, **10**, 2157–2168.

Schwartz, M., N. Livesey, W. Read, and R. Fuller, 2024: MLS/Aura Level 3 Monthly Binned Temperature on Assorted Grids V005, Greenbelt, MD, USA, Goddard Earth Sciences Data and Information Services Center (GES DISC), Accessed: [1 January 2024], 10.5067/Aura/MLS/DATA/3550

Schwartz, M., N. Livesey, W. Read, and R. Fuller, 2024: MLS/Aura Level 3 Monthly Binned Geopotential Height (GPH) on Assorted Grids V005, Greenbelt, MD, USA, Goddard Earth Sciences Data and Information Services Center (GES DISC), Accessed: [1 January 2024], 10.5067/Aura/MLS/DATA/3537

Shibata K., and M. Deushi, 2005: Partitioning between resolved wave forcing and unresolved gravity wave forcing to the quasi-biennial oscillation as revealed with a coupled chemistry-climate model. *Geophys. Res. Lett.*, **32**, L12820, doi:10.1029/2005GL022885.

Shibata, K., and M. Deushi, 2012: Future changes in the quasi-biennial oscillation under a greenhouse gas increase and ozone recovery in transient simulations by a chemistry-climate model. *Greenhouse Gases - Emission, Measurement and Management*. Liu, G. (ed.), InTech, 355–386.

Shibata, K., and H. Naoe, 2022: Decadal amplitude modulations of the stratospheric quasi-biennial oscillation. *J. Meteor. Soc. Japan*, **100**, 29–44.

Shibata, K., and H. Naoe, 2025: Structure, trends and variabilities of the semiannual oscillation in the equatorial middle atmosphere analyzed in the Japanese Reanalysis of Three Quarters of a Century (JRA-3Q). (revised) *J. Meteor. Soc. Japan*.

Smith, A. K., R. R. Garcia, A. C. Moss, and N. J. Mitchell, 2017: The semiannual oscillation of the tropical zonal wind in the middle atmosphere derived from satellite geopotential height retrievals. *J. Atmos. Sci.*, **74**, 2413–2425.

SPARC, 2022: SPARC Reanalysis Intercomparison Project (S-RIP) Final Report. Fujiwara, M., G. L., Manney, L. J. Gray, and J. S. Wright (Eds.), SPARC Report No. 10, WCRP-6/2021, 612pp. doi: 10.17874/800dee57d13. [Available online at https://www.sparc-climate.org/sparc-report-no-10/, accessed 13 June 2022]

Takahashi, M., 1996: Simulation of the stratospheric quasi-biennial oscillation using a general circulation model. *Geophys. Res. Lett.*, **23**, 661–664.

Tegtmeier, S., J. Anstey, S. Davis, R. Dragani, Y. Harada, I. Ivanciu, R. P. Kedzierski, K. Krüger, B. Legras, C. Long, J. S. Wang, K, Wargan, and J. S. Wright, 2020: Zonal Asymmetry of the QBO Temperature Signal in the Tropical Tropopause Region. *Geophys. Res. Lett.*, **47**, e2020GL089533, doi: 10.1029/2020GL089533.

Torrence, C. and G. P. Compo, 1998: A practical guide to wavelet analysis. *Bull. Amer. Meteor. Soc.*, **79**, 61–78.

Watanabe S., Y. Kawatani, Y. Tomikawa, K. Miyazaki, M. Takahashi, and K. Sato, 2008:

General aspects of a T213L256 middle atmosphere general circulation model. *J. Geophys. Res.*, **113**, D12110, doi:10.1029/2008JD010026.

List of Figures

Fig. 1. Time series of monthly zonal-mean zonal wind averaged over 5°S and 5°N for (a) JRA-3Q, (b) JRA-55, (c) ERA5, (d) MERRA-2, (e) AURA/MLS (AMLS), and (e) combined radiosonde observations at the equator. AMLS zonal wind is estimated from the geostrophic balance using the AMLS monthly 3D temperature field. Radiosonde data are derived from three stations: Canton Island (2.8°S, 171.7°W) from 1953 to 1967, Gan/Maldives (0.7°S, 73.15°E) from 1967 to 1975, and Singapore (1.4°N, 103.9°E) from 1953 to 2023.

Fig. 2. Power spectra of zonal-mean zonal wind averaged over 10°S and 10°N from 100 hPa to 1 hPa during a post-satellite era 2003–2022 for (a) JRA-3Q, (b) MERRA-2, and (c) ERA5. Power spectra during pre-satellite eras for (d) 1948–1967 JRA-3Q, (e) 1958–1977 JRA-55 and (f) 1948–1967 ERA5. Values are displayed on a logarithmic scale of base 10 and are expressed in units of m^2 s^{-2}. The contour interval is 0.4.

Fig. 3. (a) Wavelet power spectrum of zonal-mean zonal wind at the equator (5°S–5°N) at 20 hPa in JRA-3Q. The thin gray line represents the mean red noise spectrum (theoretical background noise) with an AR(1) of 0.94. The upper thick gray line represents the 95% confidence spectrum, assuming the square of a normally distributed variable being chi-square distributed with one DOF for each real and imaginary part of the complex wavelet

transform function. A green line indicates the spectrum of zonal wind power taken at time January 2010, normalized by variance. (b) The 21-year averaged power spectrum along with the 95% confidence level, and the DOF is increased by averaging in time and scale.

Fig. 4. Time series of the wavelet power spectrum of zonal-mean zonal wind at 20 hPa at the equator (5°S–5°N) over the period ranging from 9 to 60 months. The COI is represented by cross hatching.

Fig. 5. Time series profile of wavelet power amplitude of zonal wind (m s^{-1}) for (a) JRA-3Q, (b) JRA-55, (c) ERA5, (d) MERRA-2, (e) AMLS, and (f) the sonde data. The QBO is defined in wavelet power spectrum from 20 to 40 months, and the power amplitude is considered to be square root of twice the power. The dot indicates the confidence below the 95% level, based on the background red noise taken from the post-satellite era from 1980 to 2022.

Fig. 6. Wavelet power amplitude (blue) and direct-method amplitude (red) of zonal-mean zonal wind QBO (m s^{-1}) at 20 hPa in JRA-3Q. A black solid line represents the absolute of band-pass filtered data averaged between 5°S and 5°N, with star marks indicating the minimum of the square of the band-passed data. A horizontal gray line denotes the 95% confidence level of the wavelet power over the range of 20 to 40 months.

Fig. 7. Time series of wavelet power amplitude for (a) zonal wine at 20 hPa and (b) temperature at 30 hPa for JRA-3Q (red), JRA-55 (blue), ERA5 (green), MERRA-2 (yellow), AMLS (orange), and sonde observations (purple). The gray horizontal line represents the 95% confidence level of the red noise averaged over the four reanalysis datasets, evaluated from data spanning 1980–2022. The solid part of the horizontal line covers the period from 1982 to 2020, while the dashed part covers the period from 1940 to 1981 and after 2020.

Fig. 8. (a) Time series of the average period (months) of the three largest components in the local wavelet power of the zonal-mean zonal wind at 20 hPa for (a) JRA-3Q (black), along with a linear regression (red) during the period from 1982 to 2020. (b) Same as (a) but for the radiosonde observations (gray), with a linear regression (purple). (c) QBO amplitude of zonal wind (m s^{-1}) at 20 hPa by the wavelet method for JRA-3Q and radiosonde observations. (d) Same as (a) but for zonal-mean temperature at 10 hPa. (e) Same as (b) but for ERA5 (gray) with a linear regression (green). (f) Same as (c) but for QBO amplitude of temperature (K) at 10 hPa for JRA-3Q and ERA5.

Fig. 9. Vertical profile of trends in (a) QBO amplitude and (b) power-peak period of zonal wind at the equator during the satellite era from 1982 to 2020. Data are presented for

JRA-3Q, JRA-55, ERA5, MERRA-2, and the radiosonde observations. Circles stand for the statistical significance at the 95% level. The effective decorrelation time for the QBO is assumed to be 14 months. (c) and (d), same as (a) and (b) but for temperature.

Fig. 10. Time-series of the seasonal march of zonal-mean zonal wind at 20 hPa. The x-axis spans 25 months to visualize the seasonal march of the QBO, while the y-axis represents data every two years. (a) JRA-3Q, (b) JRA-55, (c) ERA5, (d) AMLS, and (e) JRA-55C.

Fig. 11. (a) Latitude-height cross section of zonal wind QBO amplitude (m s^{-1}) in a satellite-era period from 1982 to 2020 for JRA-3Q. The dot stands for the confidence level below 95%. (b) Latitudinal profiles of the zonal wind QBO amplitude at 20 hPa during the same period for JRA-3Q (red), JRA-55 (blue), ERA5 (green), MERRA-2 (yellow), and AMLS (orange), along with the mean 95% confidence level derived from the mean of four reanalyses (gray). The period covered by MLS is from 2007 to 2020 to avoid data edges. (c, d) Same as (a, b) but for zonal mean temperature QBO amplitude (K).

Fig. 12. Longitude-height cross section of QBO amplitude of zonal wind (m s^{-1}) at the equator during the satellite era from 1982 to 2022 for (a) JRA-3Q, (b) JRA-55, (c) ERA5, and (d) MERRA-2. Shadings indicate anomalies from the zonal mean.

Fig. 13. Same as Fig. 12, but for QBO amplitude of temperature (K).

Supplement figure captions

Fig. S1. Power spectra of zonal-mean temperature averaged over 10°S and 10°N from 100 hPa to 1 hPa during a post-satellite era 2003–2022 for (a) JRA-3Q, (b) MERRA-2, and (c) ERA5. Power spectra during pre-satellite eras for (d) 1948–1967 JRA-3Q, (e) 1958–1977 JRA-55, and (f) 1948–1967 ERA5. Values are shown on a logarithmic scale of base 10, and are expressed in units of K^2. The contour interval is 0.4.

Fig. S2. Time series of wavelet power amplitude profile of temperature (K) for (a) JRA-3Q, (b) JRA-55, (c) ERA5, (d) MERRA-2, and (e) AMLS. The QBO is defined in the wavelet power spectrum from 20 to 40 months, with the power amplitude assumed to be square root of twice the power. The dot indicates the confidence below the 95% level, based on the background red noise taken from the post-satellite era from 1980 to 2022.

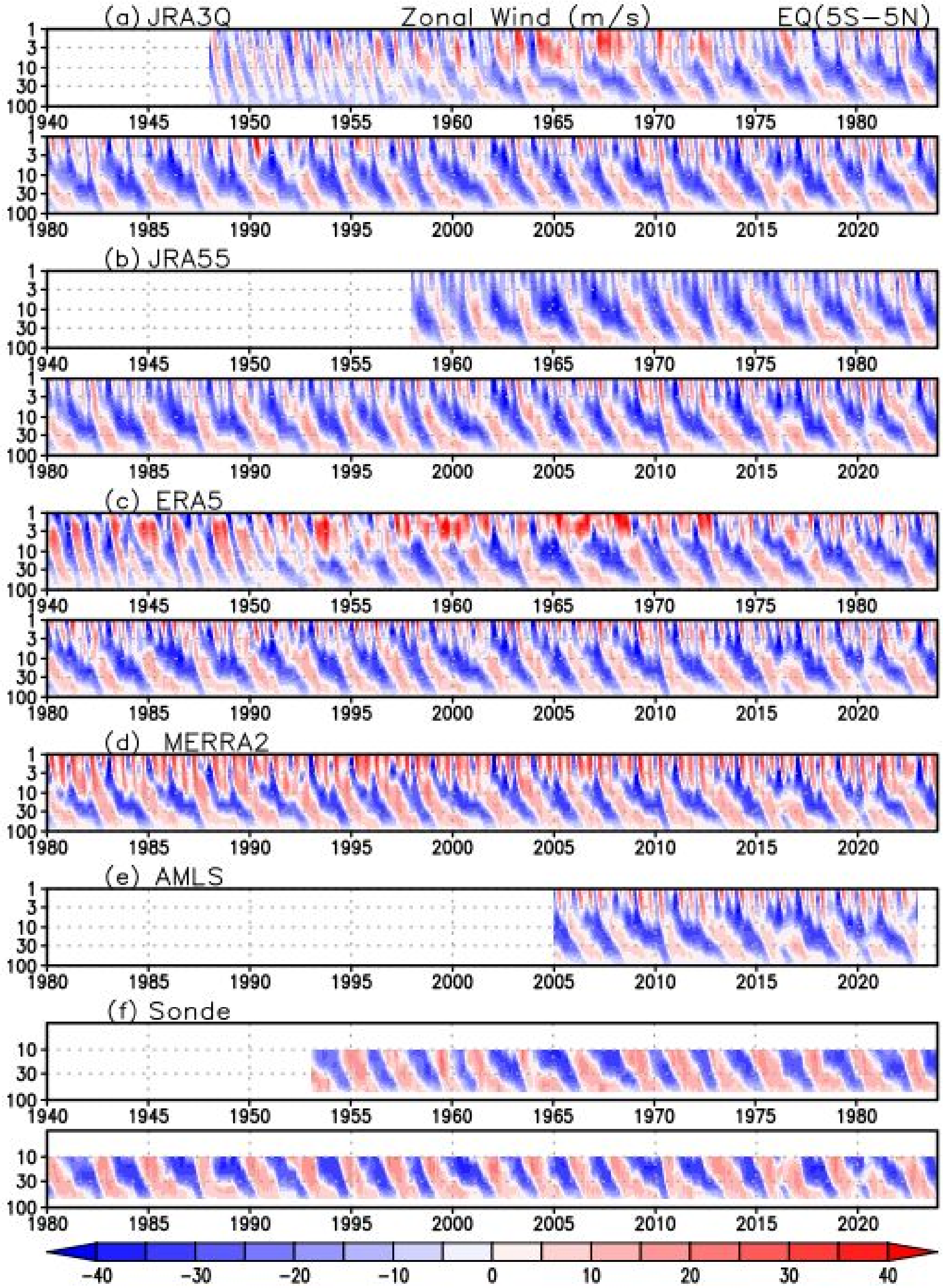

Fig. 1. Time series of monthly zonal-mean zonal wind averaged over 5°S and 5°N for (a) JRA-3Q, (b) JRA-55, (c) ERA5, (d) MERRA-2, (e) AURA/MLS (AMLS), and (e) combined radiosonde observations at the equator. AMLS zonal wind is estimated from the geostrophic balance using the AMLS monthly 3D temperature field. Radiosonde data are from three stations: Canton Island (2.8°S, 171.7°W) from 1953 to 1967, Gan/Maldives (0.7°S, 73.15°E) from 1967 to 1975, and Singapore (1.4°N, 103.9°E) from 1953 to 2023.

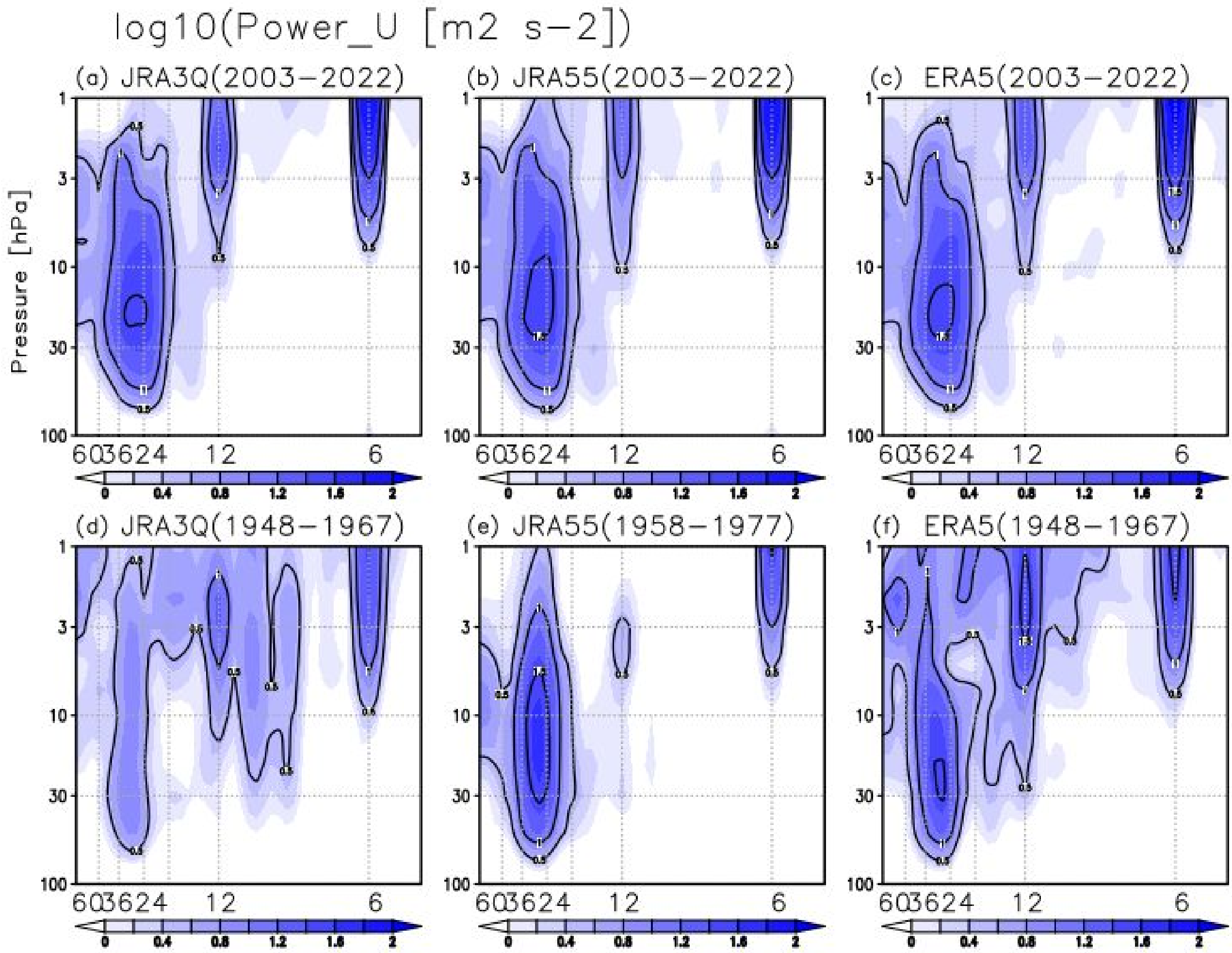

Fig. 2. Power spectra of zonal-mean zonal wind averaged over 10°S and 10°N from 100 hPa to 1 hPa during a post-satellite era 2003–2022 for (a) JRA-3Q, (b) MERRA-2, and (c) ERA5. Power spectra during pre-satellite eras for (d) 1948–1967 JRA-3Q, (e) 1958–1977 JRA-55 and (f) 1948–1967 ERA5. Values are expressed in a logarithmic scale of base 10 in units of $m^2 s^{-2}$. The contour interval is 0.4.

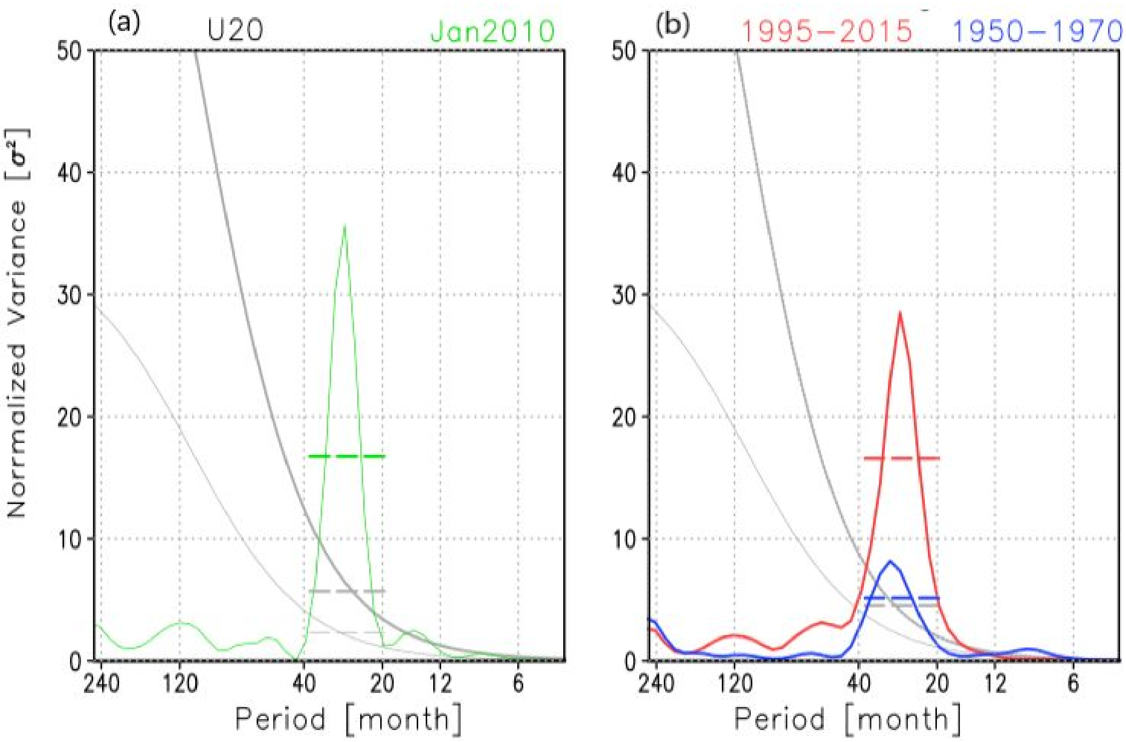

Fig. 3. (a) Wavelet power spectrum of zonal mean zonal wind at the equator (5°S–5°N) at 20 hPa in JRA-3Q. The thin gray line represents the mean red noise spectrum (theoretical background noise) with an AR(1) of 0.94. The upper thick gray line represents the 95% confidence spectrum assuming the square of a normally distributed variable being chi-square distributed with one DOF for each real and imaginary part of the complex wavelet transform function. A green line indicates a spectrum of zonal wind power taken at time January 2010, normalized by variance. (b) The 21-year averaged power spectrum along with the 95% confidence level, and the DOF is increased by averaging in time and scale.

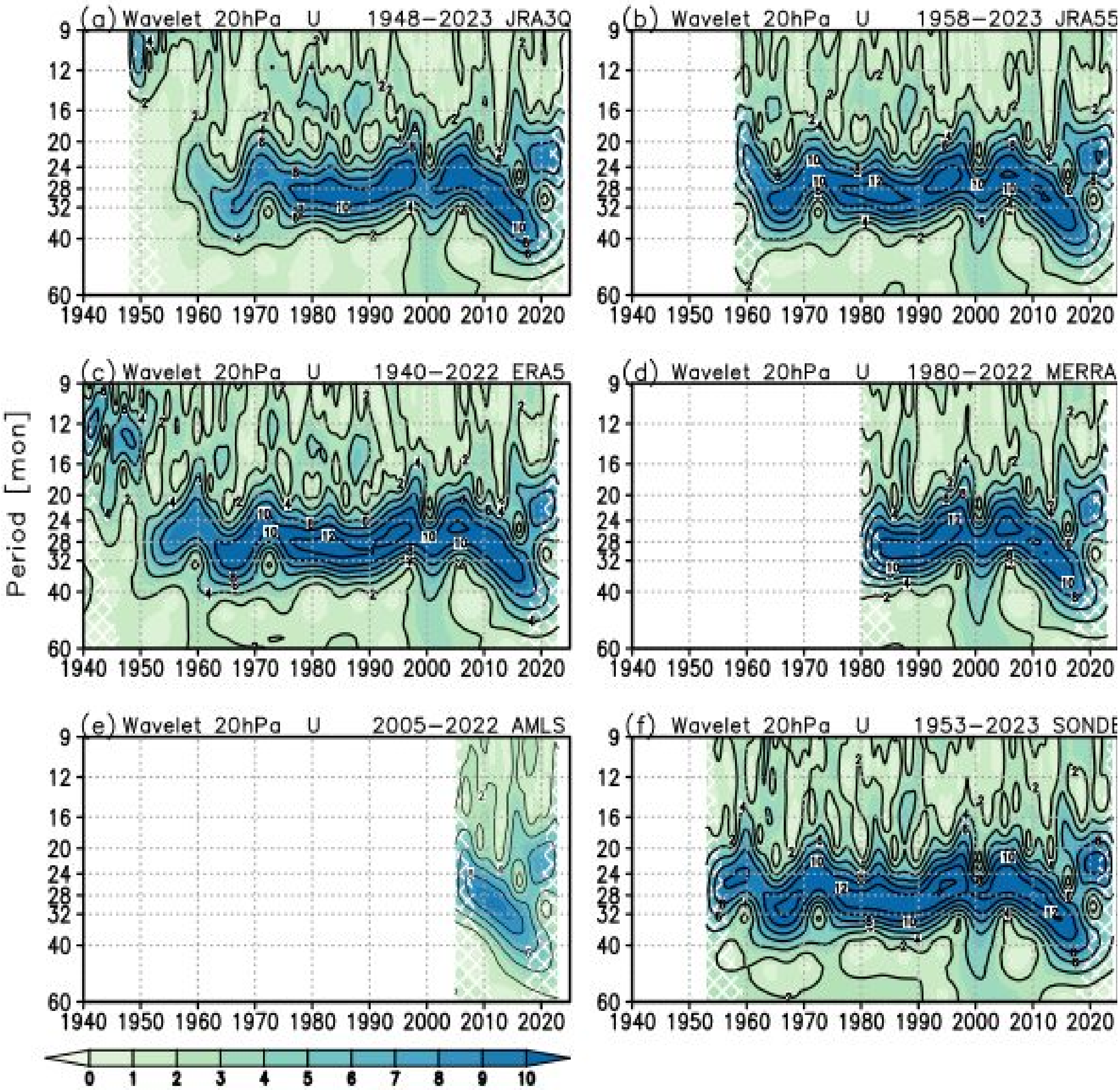

Fig. 4. Time series of the wavelet power spectrum of zonal-mean zonal wind at 20 hPa at the equator (5°S–5°N) over the period ranging from 9 to 60 months. The COI is represented by cross hatching.

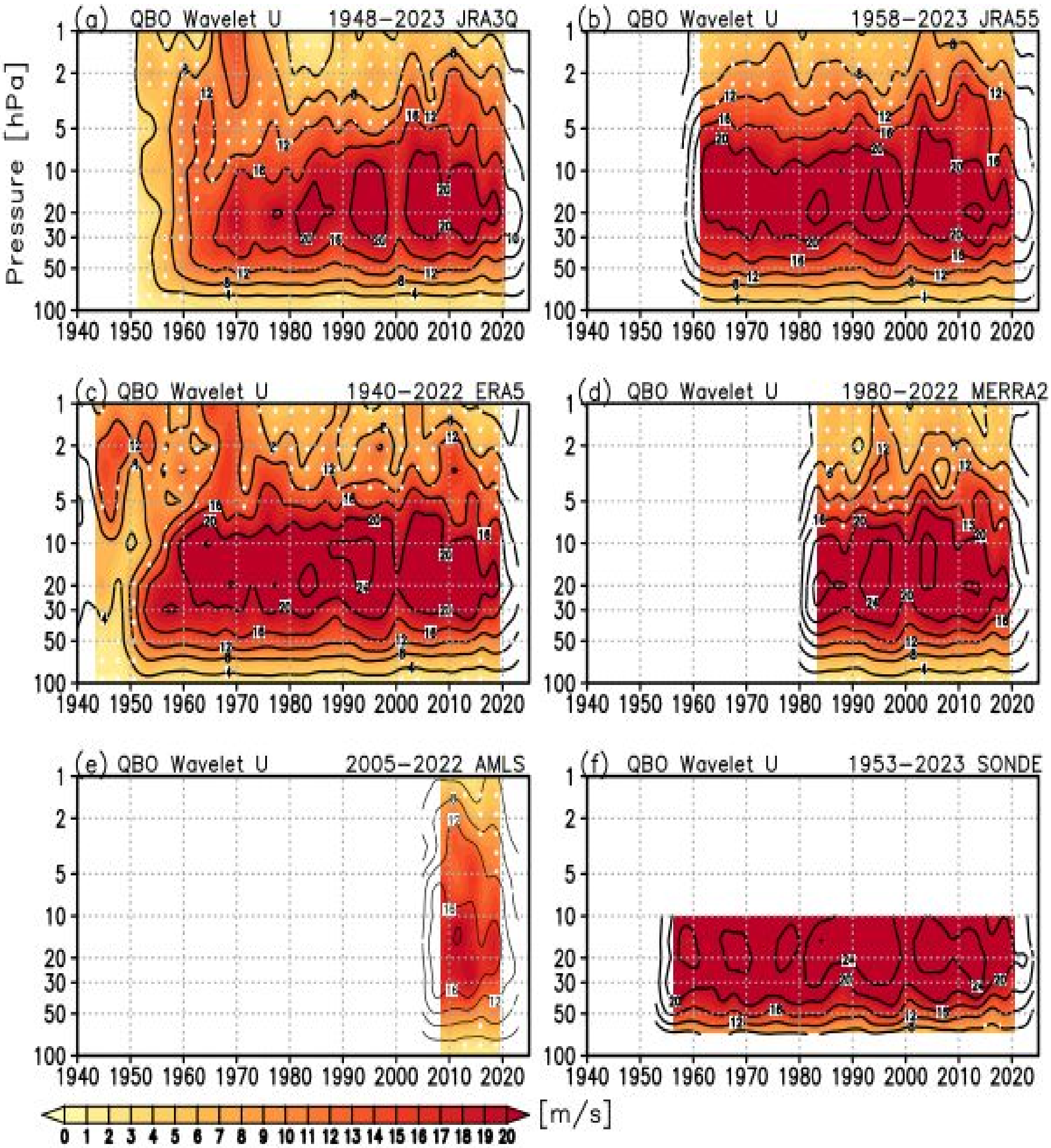

Fig. 5. Time series of wavelet power amplitude profile of zonal wind (m s^{-1}) for (a) JRA-3Q, (b) JRA-55, (c) ERA5, (d) MERRA-2, (e) AMLS, and (f) the sonde data. The QBO is defined in wavelet power spectrum from 20 to 40 months, with the power amplitude assumed to be square root of twice the power. The dot indicates the confidence below the 95% level, based on the background red noise taken from the post-satellite era from 1980 to 2022.

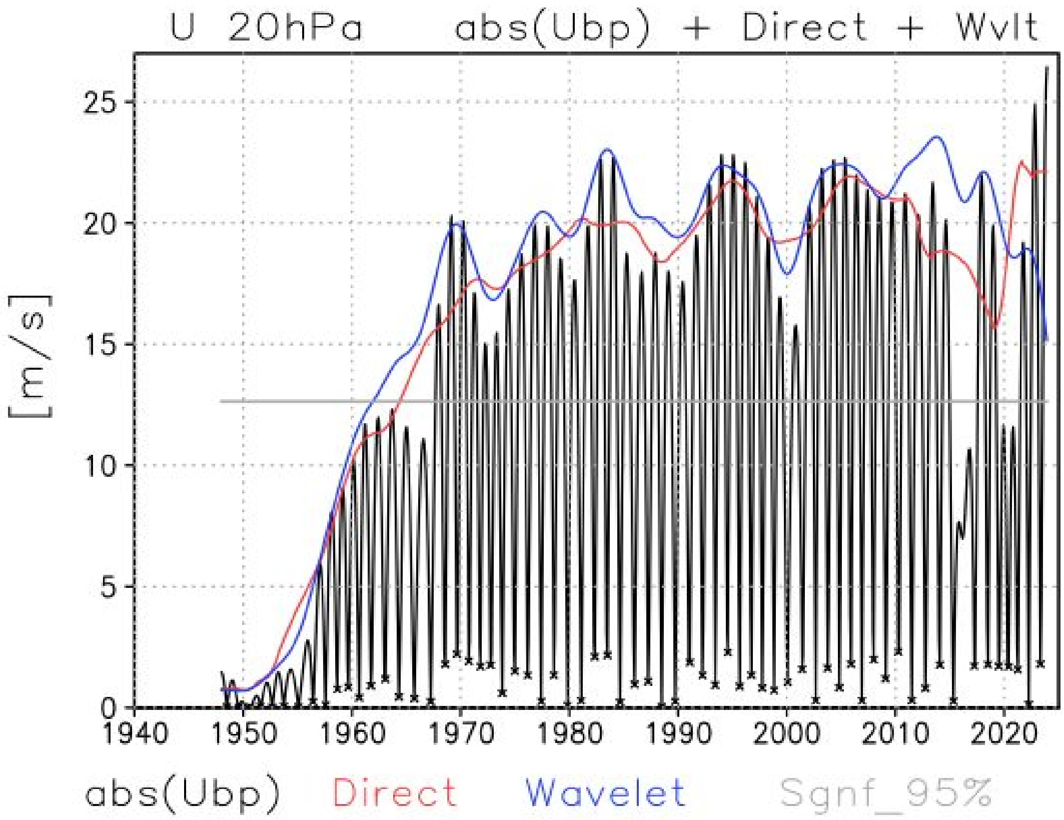

Fig. 6. Wavelet power amplitude (blue) and direct-method amplitude (red) of zonal-mean zonal wind QBO (m s^{-1}) at 20 hPa in JRA-3Q. A black solid line represents the absolute of band pass filtered data averaged between 5°S and 5°N, with star marks indicating the minimum of the square of the band-passed data. A horizontal gray line denotes the 95% confidence level of the wavelet power over the range of 20 to 40 months.

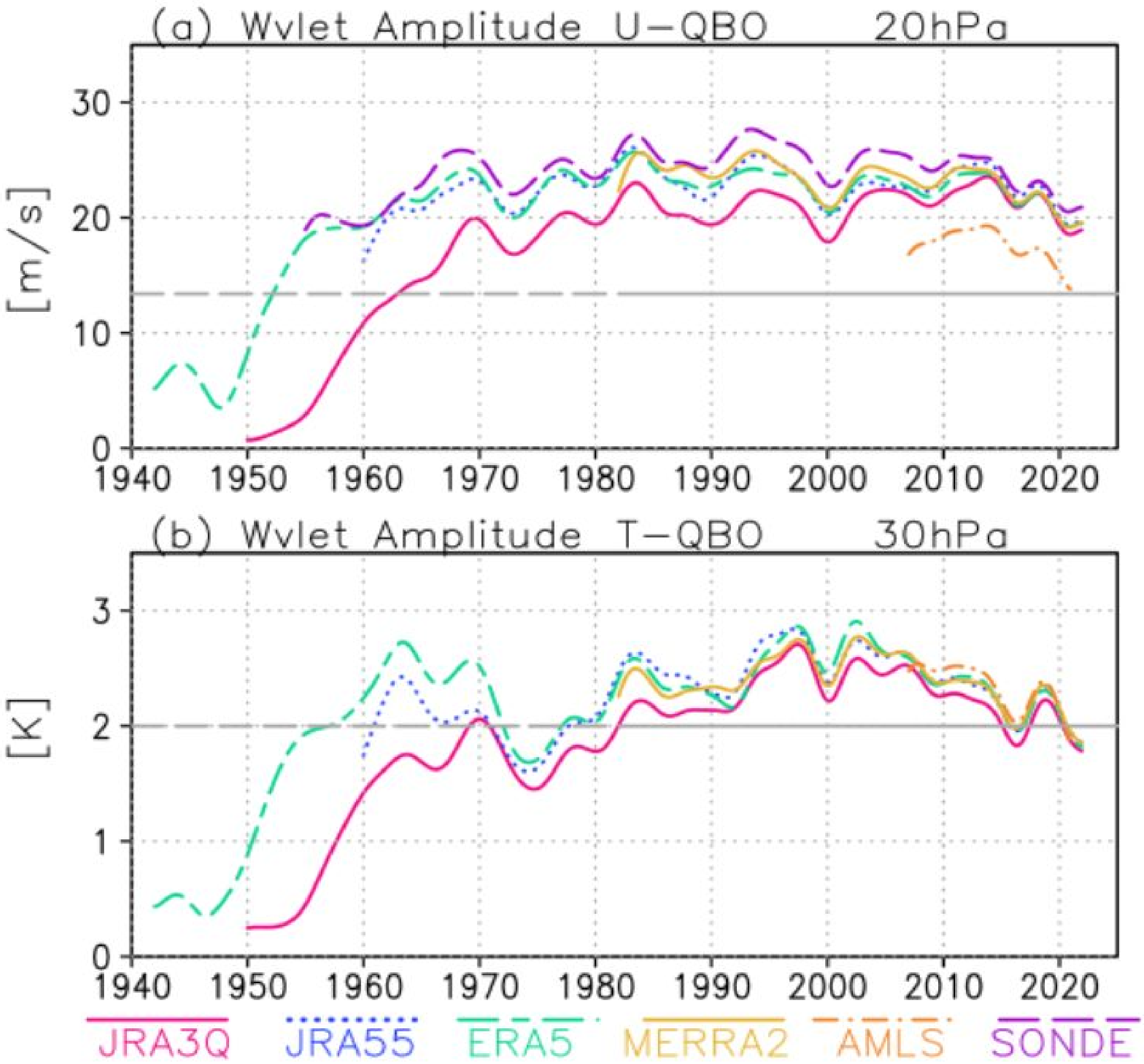

Fig. 7. Time series of wavelet power amplitude for (a) zonal wine at 20 hPa and (b) temperature at 30 hPa for JRA-3Q (solid magenta), JRA-55 (dotted blue), ERA5 (long short dash aqua), MERRA-2 (solid yellow), AMLS (dot dash orange), and sonde observations (long dash purple). The gray horizontal line represents the 95% confidence level of the red noise averaged over the four reanalysis datasets, evaluated from data spanning 1980–2022. The solid part of the horizontal line covers the period from 1982 to 2020, while the dashed part covers the period from 1940 to 1981 and after 2020.

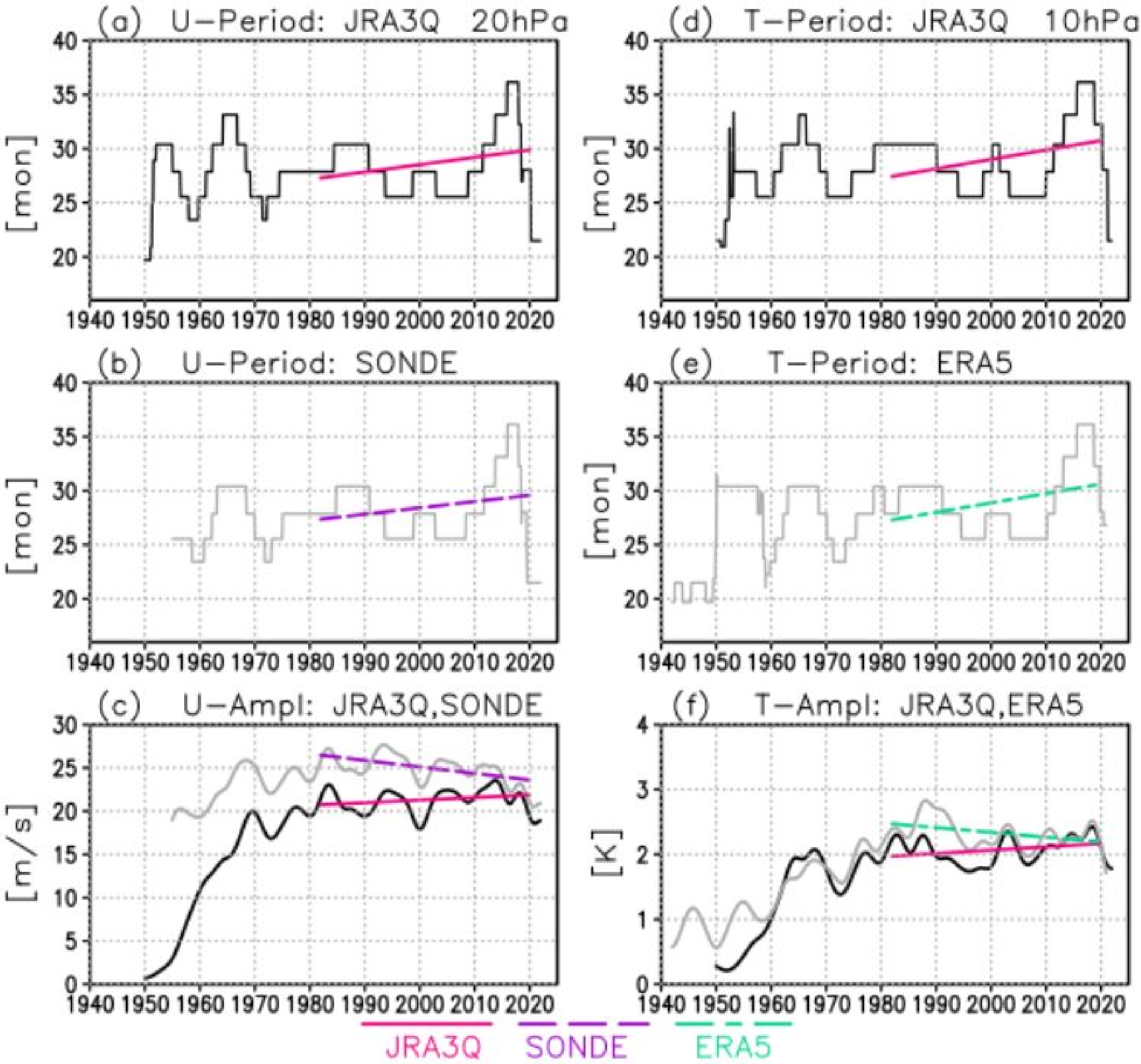

Fig. 8. (a) Time series of the average period (months) of the three largest components in the local wavelet power of the zonal-mean zonal wind at 20 hPa for (a) JRA-3Q (black), along with a linear regression (magenta) during the period from 1982 to 2020. (b) Same as (a) but for radiosonde observations (gray) with a linear regression (purple). (c) QBO amplitude of zonal wind (m s^{-1}) at 20 hPa by the wavelet method for JRA-3Q and radiosonde observations. (d) Same as (a) but for zonal-mean temperature at 10 hPa. (e) Same as (b) but for ERA5 (gray) with a linear regression (aqua). (f) Same as (c) but for QBO amplitude of temperature (K) at 10 hPa for JRA-3Q and ERA5.

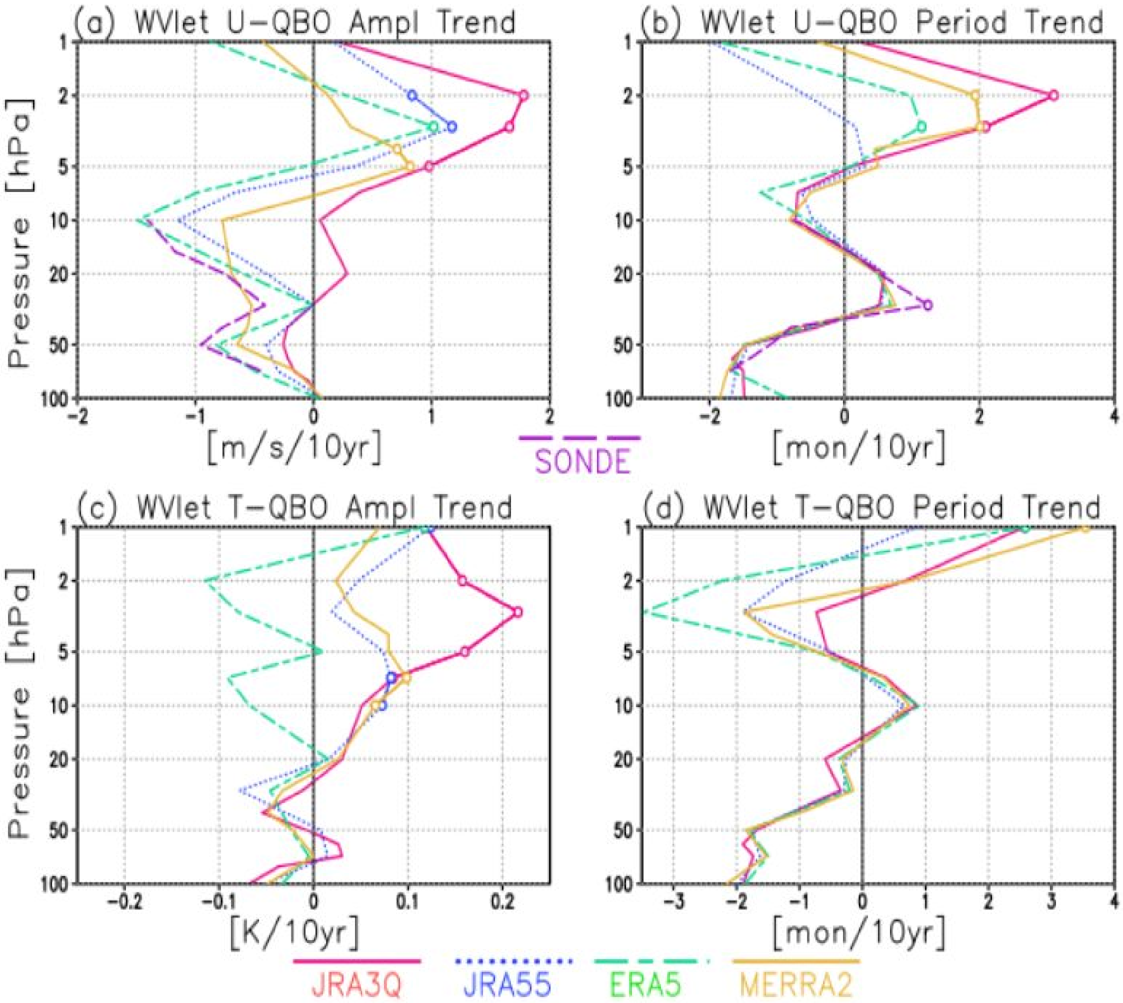

Fig. 9. Vertical profile of trends in (a) QBO amplitude and (b) power-peak period of zonal wind at the equator during the satellite era from 1982 to 2020 for JRA-3Q, JRA-55, ERA5, MERRA-2, and radiosonde observations. Circles stands for the statistical significance at the 95% level. The effective decorrelation time for the QBO is assumed to be 14 months. (c) and (d), same as (a) and (b) but for temperature.

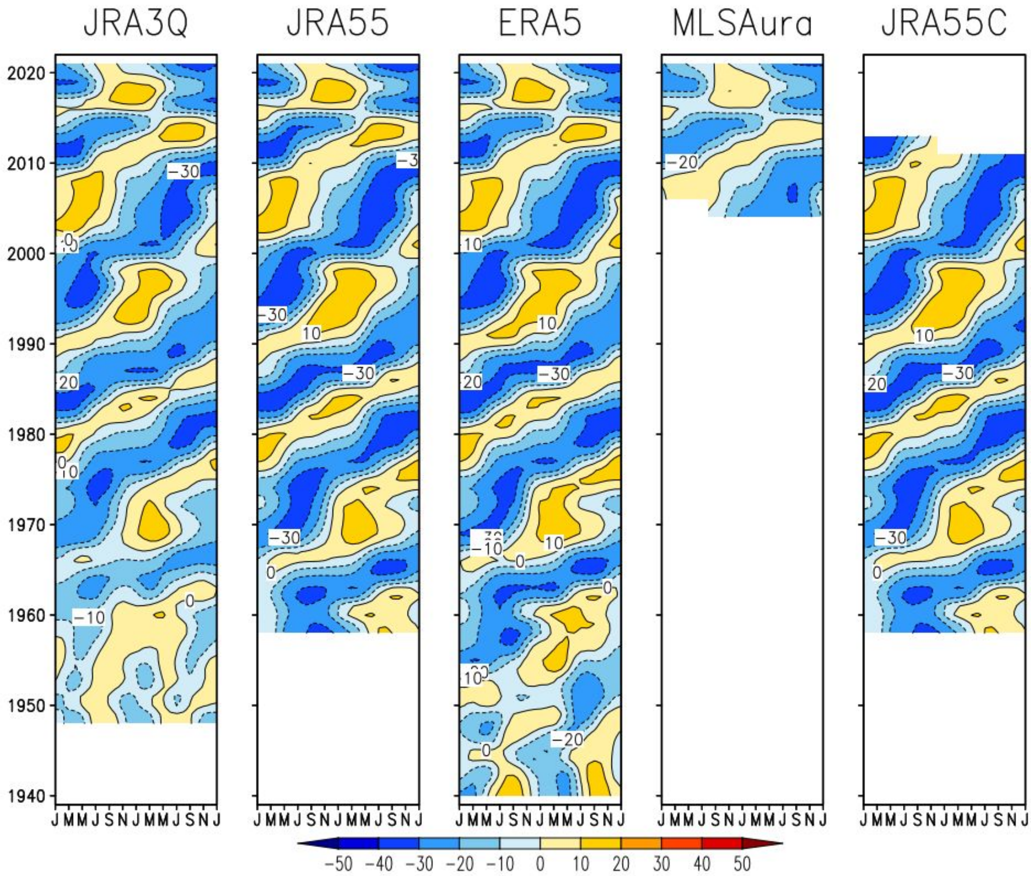

Fig. 10. Time-series of the seasonal march of zonal-mean zonal wind at 20 hPa. The x-axis spans 25 months to visualize the seasonal march of the QBO, while the y-axis represent data every two years. (a) JRA-3Q, (b) JRA-55, (c) ERA5, (d) AMLS, and (e) JRA-55C.

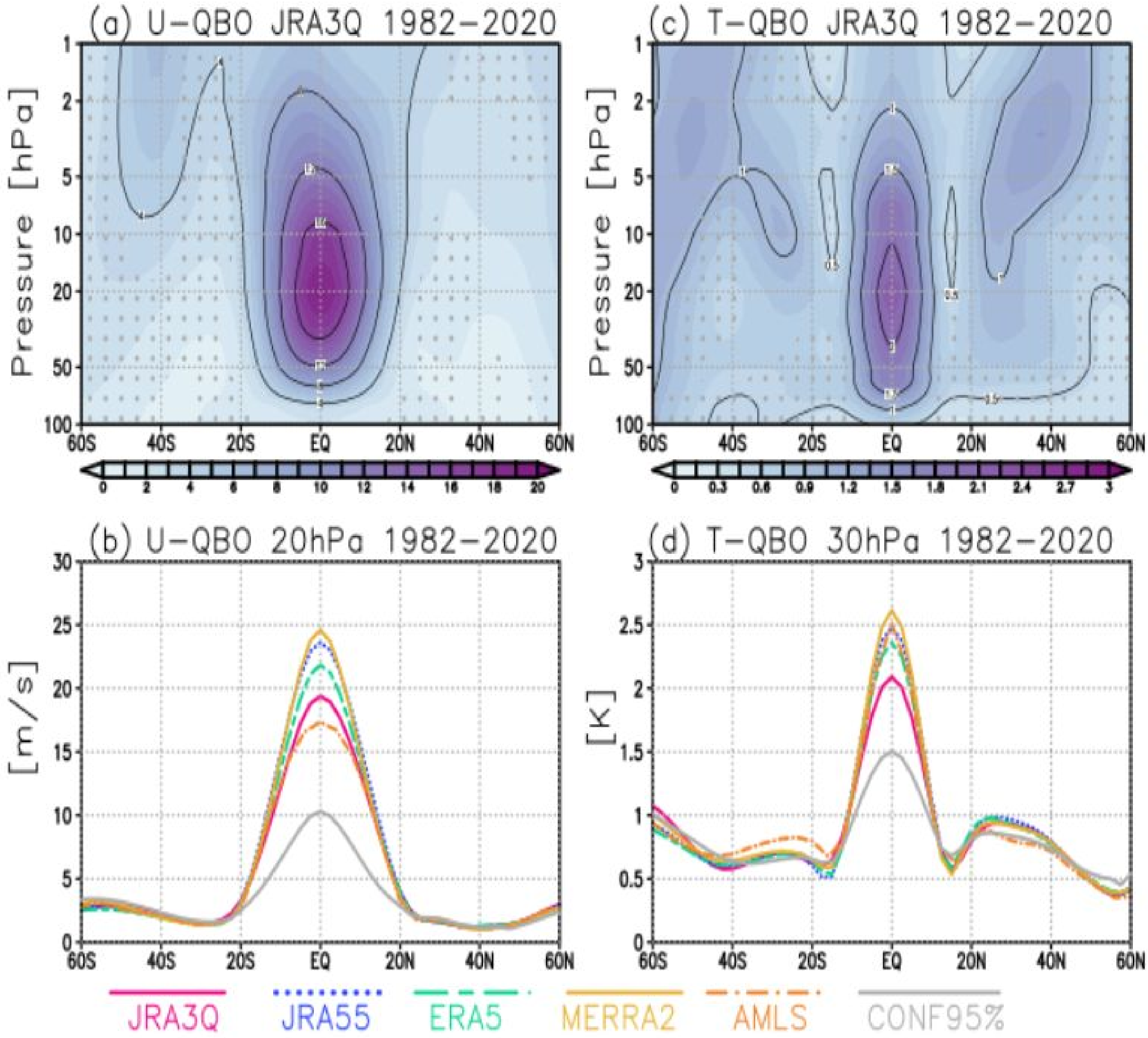

Fig. 11. (a) Latitude-height cross section of zonal wind QBO amplitude (m s^{-1}) in a satellite-era period from 1982 to 2020 for JRA-3Q. The dot stands for the confidence level below 95%. (b) Latitudinal profiles of the zonal wind QBO amplitude at 20 hPa during the same period for JRA-3Q (solid magenta), JRA-55 (dotted blue), ERA5 (long short dash aqua), MERRA-2 (solid yellow), and AMLS (dot dash orange), along with the 95% confidence level derived from the mean of four reanalyses (gray). The period covered by MLS is from 2007 to 2020 to avoid data edges. (c, d) Same as (a, b) but for zonal mean temperature QBO amplitude (K).

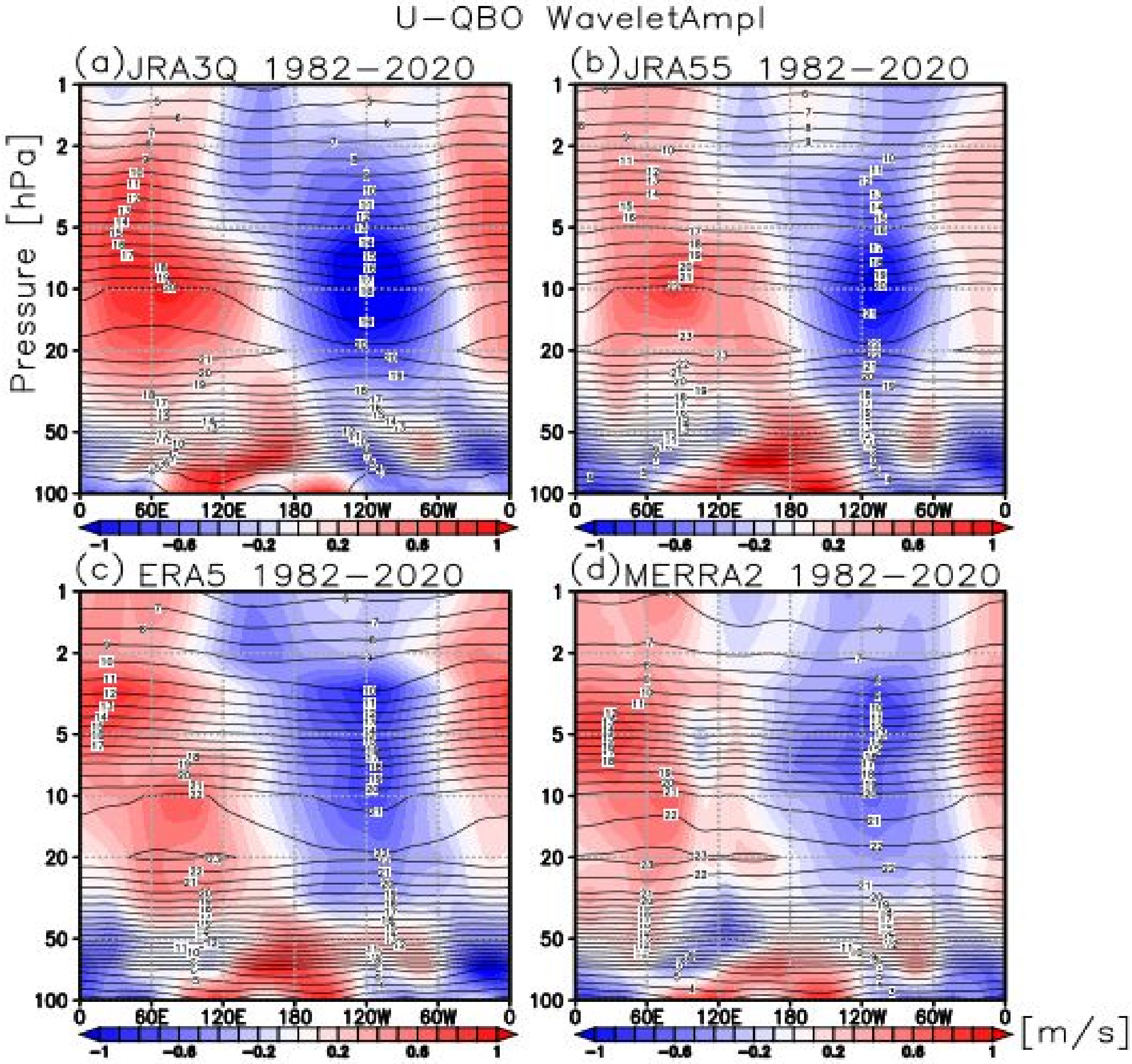

Fig. 12. Longitude-height cross section of QBO amplitude of zonal wind (m s^{-1}) at the equator during the satellite era from 1982 to 2022 for (a) JRA-3Q, (b) JRA-55, (c) ERA5, and (d) MERRA-2. Shadings indicate anomalies from the zonal mean.

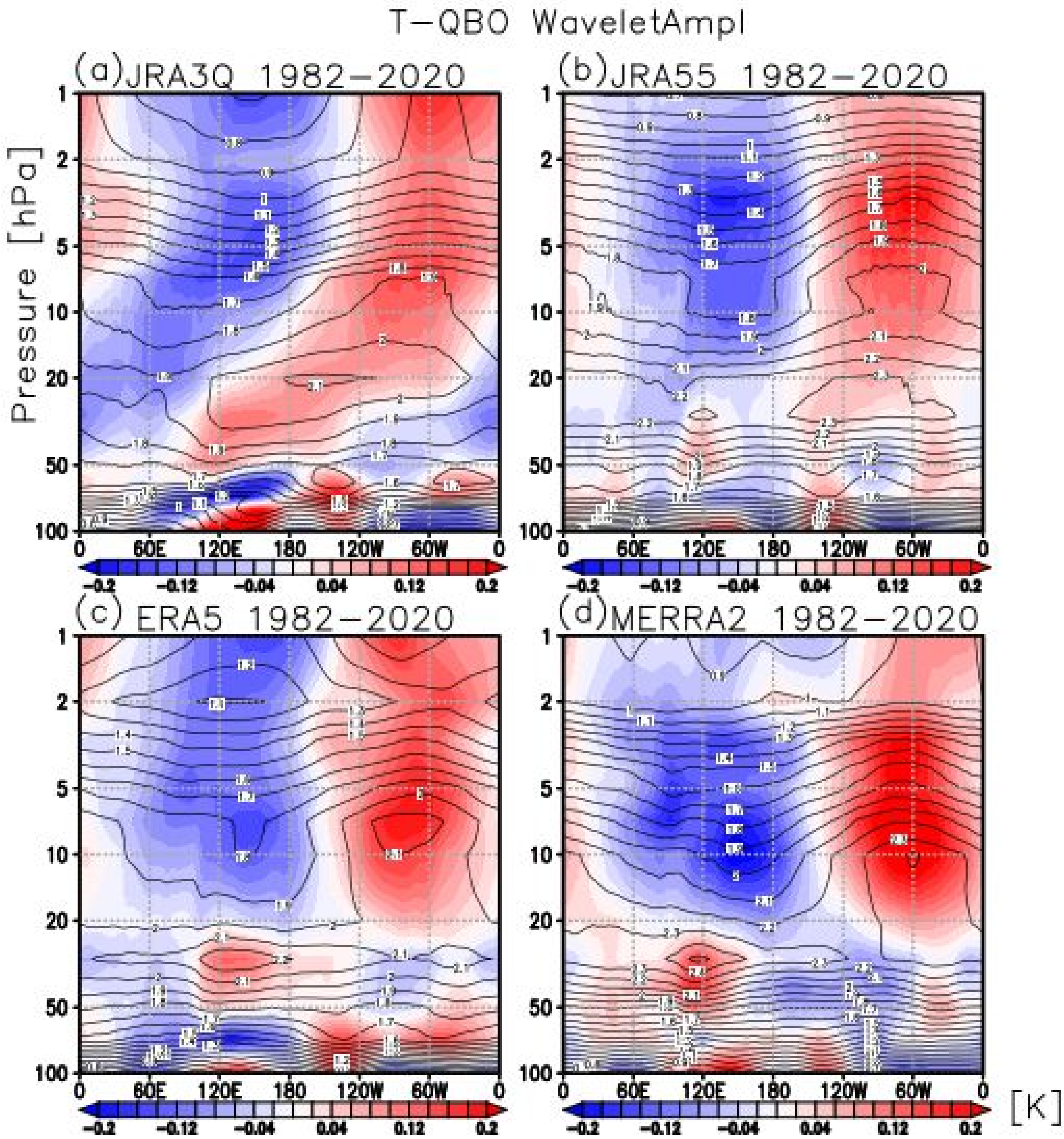

1111

1112

1113 Fig. 13. Same as Fig. 12, but for QBO amplitude of temperature (K).

1114

1115

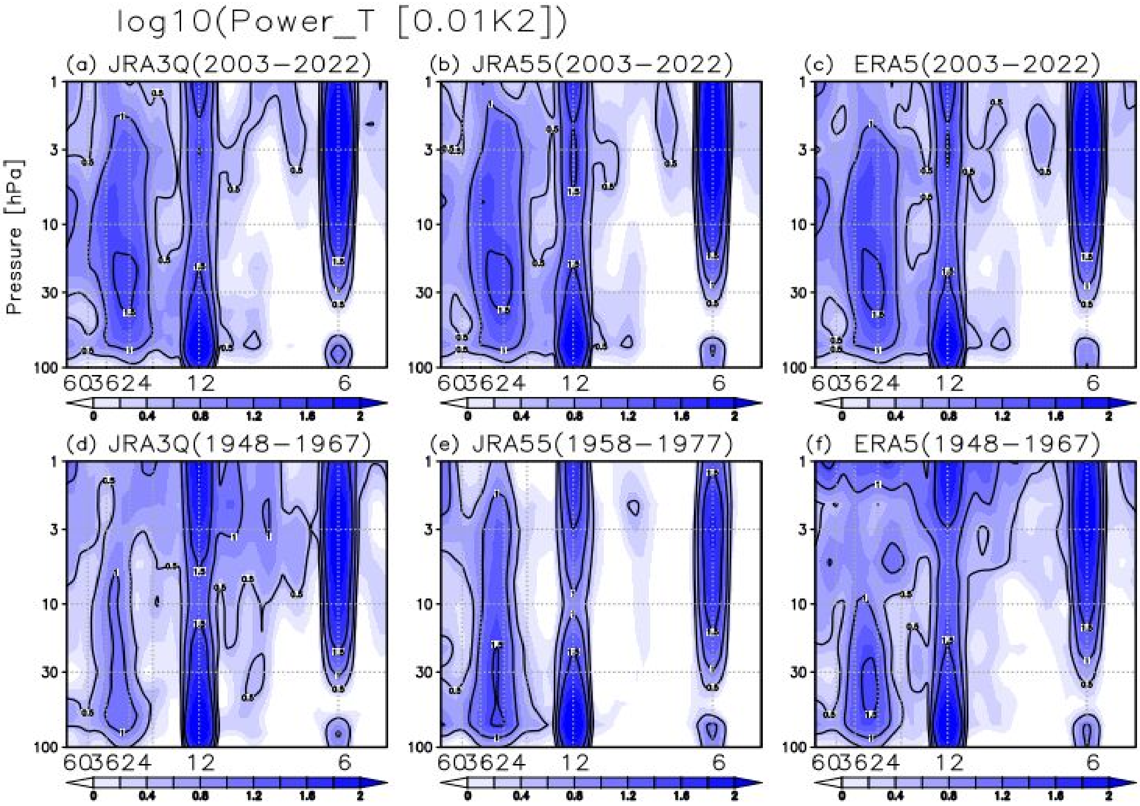

(Supplement figure)

Fig. S1. Power spectra of zonal-mean temperature averaged over 10°S and 10°N from 100 hPa to 1 hPa during a post-satellite era 2003–2022 for (a) JRA-3Q, (b) MERRA-2, and (c) ERA5. Power spectra during pre-satellite eras for (d) 1948–1967 JRA-3Q, (e) 1958–1977 JRA-55 and (f) 1948–1967 ERA5. Values are shown on a logarithmic scale of base 10, and are expressed in units of K^2. The contour interval is 0.4.

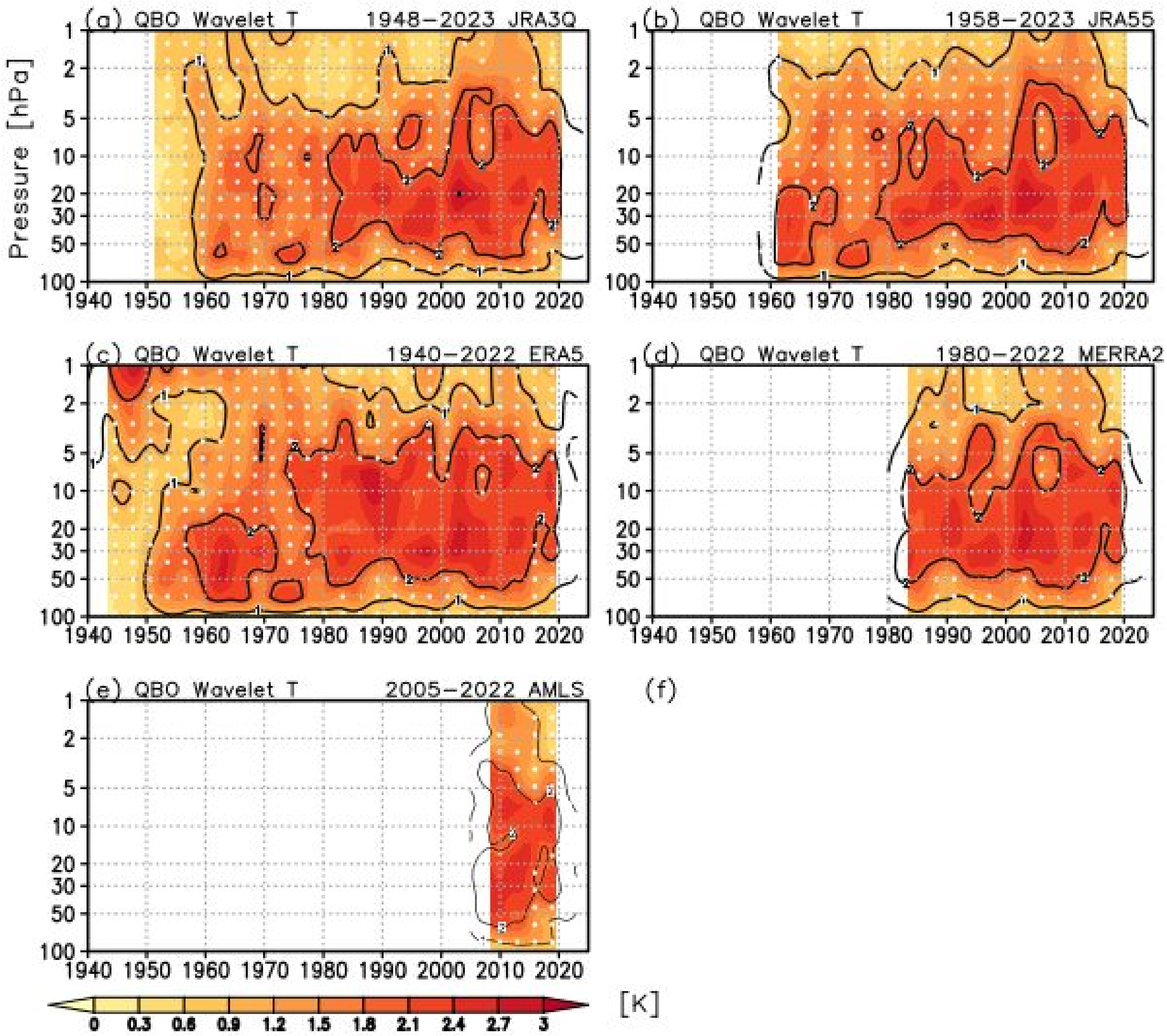

(Supplement figure)

Fig. S2. Time series of wavelet power amplitude profile of temperature (K) for (a) JRA-3Q, (b) JRA-55, (c) ERA5, (d) MERRA-2, and (e) AMLS. The QBO is defined in the wavelet power spectrum from 20 to 40 months, with the power amplitude assumed to be square root of twice the power. The dot indicates the confidence below the 95% level, based on the background red noise taken from the post-satellite era from 1980 to 2022.